

A Mastcam Multispectral Investigation of Rock Variability in Gale Crater, Mars: Implications for Alteration in the Clay-Sulfate Transition of Mount Sharp

A. M. Eng¹ , M. S. Rice¹ , W. H. Farrand² , J. R. Johnson³ , S. Jacob⁴ , E. B. Rampe⁴ , L. Thompson⁵ , M. St. Clair⁶ , D. Applin⁷ , J. Bishop⁸ , E. Cloutis⁷ , M. Gabbert¹ , J. Haber⁹ , K. Lapo¹ , A. Rudolph⁹ , C. Seeger¹⁰ , and R. Sheppard¹¹

¹Western Washington University, Bellingham, WA, USA, ²Space Science Institute, Boulder, CO, USA, ³John Hopkins University/Applied Physics Laboratory, Laurel, MD, USA, ⁴Arizona State University, Tempe, AZ, USA, ⁵University of New Brunswick, Fredericton, NB, Canada, ⁶Million Concepts, Louisville, KY, USA, ⁷University of Winnipeg, Winnipeg, MB, Canada, ⁸SETI Institute, Mountain View, CA, USA, ⁹Smithsonian National Air and Space Museum, Washington, DC, USA, ¹⁰California Institute of Technology, Pasadena, CA, USA, ¹¹Planetary Science Institute, Tucson, AZ, USA

Key Points:

- New rock spectral classes correspond to unique geologic units. One supports the hypothesis of wet-dry cycles in the clay-sulfate transition
- Cross instrument analyses imply that Mg- and Fe- sulfates are significant in the amorphous component of the clay-sulfate transition region
- The spectral signature of hydrated Mg-sulfates in visible to near infrared reflectance spectra are easily masked by phyllosilicates and/or basalt

Supporting Information:

Supporting Information may be found in the online version of this article.

Correspondence to:

A. M. Eng,
aeng60@gatech.edu

Citation:

Eng, A. M., Rice, M. S., Farrand, W. H., Johnson, J. R., Jacob, S., Rampe, E. B., et al. (2024). A Mastcam multispectral investigation of rock variability in Gale crater, Mars: Implications for alteration in the clay-sulfate transition of Mount Sharp. *Journal of Geophysical Research: Planets*, 129, e2023JE008033. <https://doi.org/10.1029/2023JE008033>

Received 13 SEP 2023

Accepted 30 JAN 2024

Abstract Since leaving Vera Rubin ridge (VRr), the Mars Science Laboratory *Curiosity* rover has traversed through the phyllosilicate-bearing region, Glen Torridon, and the overlying Mg-sulfate-bearing strata, with excursions onto the Greenheugh Pediment and Amapari Marker Band. Each of these distinct geologic units were investigated using *Curiosity*'s Mast Camera (Mastcam) multispectral instrument which is sensitive to iron-bearing phases and some hydrated minerals. We used Mastcam spectra, in combination with chemical data from Chemistry and Mineralogy, Alpha Particle X-ray Spectrometer, and Chemistry and Camera instruments, to assess the variability of rock spectra and interpret the mineralogy and diagenesis in the clay-sulfate transition and surrounding regions. We identify four new classes of rock spectra since leaving VRr; two are inherent to dusty and pyroxene-rich surfaces on the Amapari Marker Band; one is associated with the relatively young, basaltic, Greenheugh Pediment; and the last indicates areas subjected to intense aqueous alteration with an amorphous Fe-sulfate component, primarily in the clay-sulfate transition region. To constrain the Mg-sulfate detection capabilities of Mastcam and aid in the analyses of multispectral data, we also measured the spectral response of mixtures with phyllosilicates, hydrated Mg-sulfate, and basalt in the laboratory. We find that hydrated Mg-sulfates are easily masked by other materials, requiring ≥ 90 wt.% of hydrated Mg-sulfate to exhibit a hydration signature in Mastcam spectra, which places constraints on the abundance of hydrated Mg-sulfates along the traverse. Together, these results imply significant compositional changes along the traverse since leaving VRr, and they support the hypothesis of wet-dry cycles in the clay-sulfate transition.

Plain Language Summary The clay-sulfate transition in Gale crater has long been hypothesized to record an environmental shift from “warm and wet” to “cold and dry.” The paleolake that once filled Gale crater allowed phyllosilicates to form. As Mars became cooler and drier, sulfates were able to precipitate above the phyllosilicates. This mineralogic transition has been observed in other places on Mars, implying a global environmental change. Different hydrated Mg-sulfates can reveal characteristics of the paleoenvironment at the time of deposition and thus clarify the geologic history. The goals of this study are to (a) characterize potential sulfate-bearing rocks with the *Curiosity* rover's multispectral imaging instrument, Mastcam; and (b) constrain Mastcam's Mg-sulfate detection threshold using laboratory techniques. We identify three new rock spectral classes inherent to the clay-sulfate transition and one new class associated with the Greenheugh pediment. Our laboratory results indicate that it would be challenging to detect Mg-sulfate with Mastcam unless it is nearly pure.

1. Introduction

In 2011, approximately 1.5 years before the launch of the Mars Science Laboratory (MSL) *Curiosity* rover, Gale crater was selected as its landing site from over 50 candidates (Golombek et al., 2012). Within Gale crater is a ~5 km sedimentary mound in the center known as Aeolis Mons (informally called Mount Sharp). Given that the primary science objective of MSL is to assess past and present habitability, Gale crater was selected for two important reasons (Grotzinger et al., 2012). First, phyllosilicate enriched sedimentary rocks on Earth are known to maintain organics. Thus, spectral signatures inherent to phyllosilicates in orbital data (Milliken et al., 2010) imply

© 2024. The Authors.

This is an open access article under the terms of the [Creative Commons Attribution License](https://creativecommons.org/licenses/by/4.0/), which permits use, distribution and reproduction in any medium, provided the original work is properly cited.

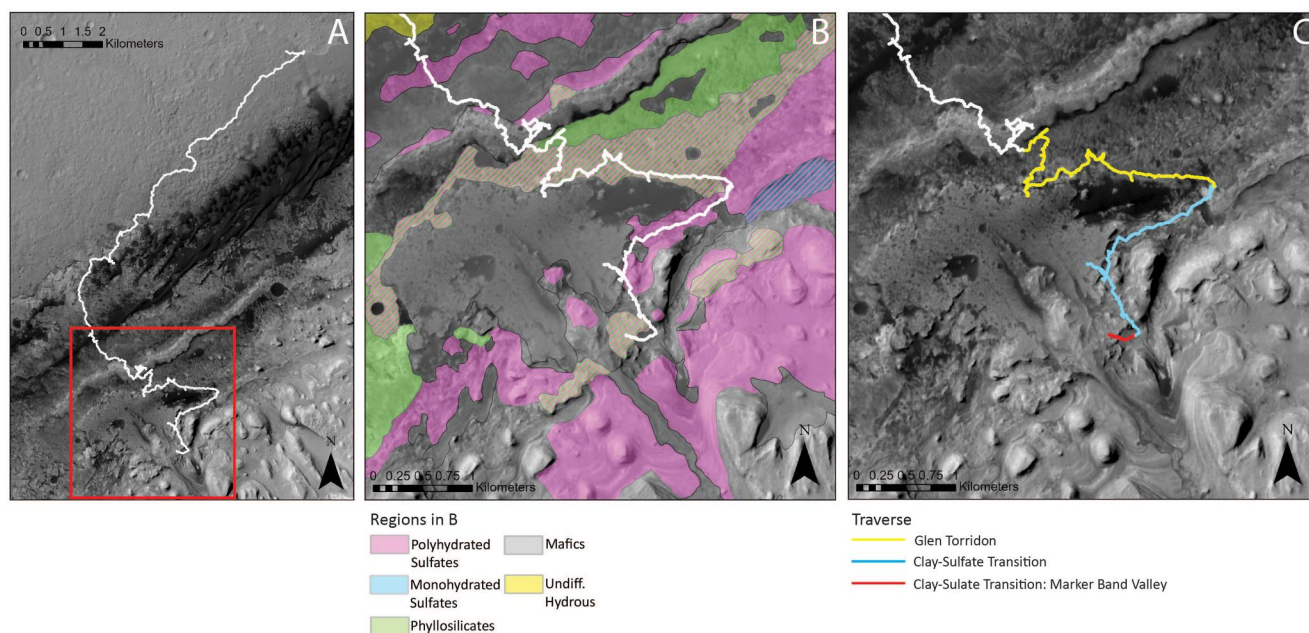


Figure 1. (a) Map of *Curiosity's* traverse over Mars Reconnaissance Orbiter Context Camera (CTX) mosaic of Gale crater through sol 3672 with more recent traverse in the red box and panels (b) and (c). (b) Map of *Curiosity's* traverse from sol \sim 1570 to 3672 with mineralogic units from Sheppard et al. (2022). (c) Traverse in color represents regions of interest in this study and corresponds to colors in stratigraphic column in Figure 2.

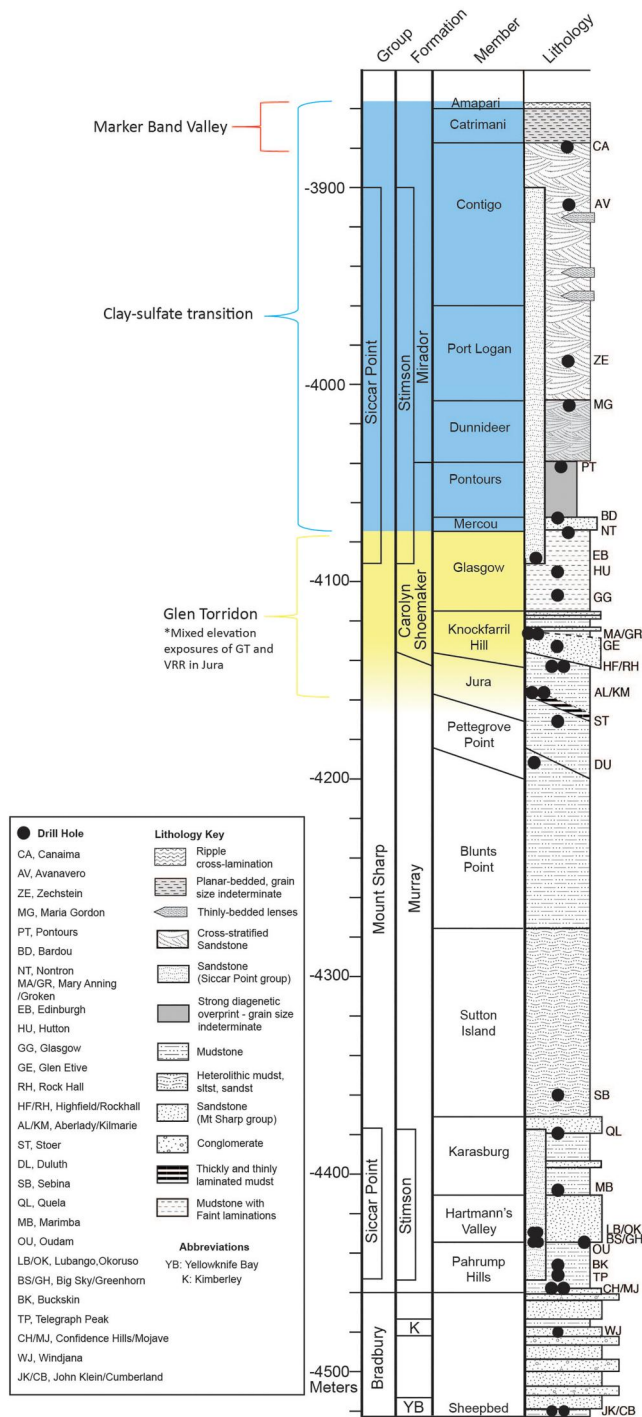
that Gale has a high potential for biologic preservation (e.g., organic carbon, see Broz, 2020), if present. Additionally, the sulfate-rich units in lower Mount Sharp may harbor biosignatures (e.g., amino acids, see Kotler, 2009), and/or S-isotopes with implications for biogeochemical S-cycling (Moreras-Marti et al., 2022). Second, the sulfate-bearing strata overlying the phyllosilicate-bearing strata in lower Mount Sharp are hypothesized to record environmental drying with time (Milliken et al., 2010; Sheppard et al., 2022) (Figure 1). Six and a half years after landing, *Curiosity* has finally traversed into the region responsible for its landing site selection.

1.1. Overview of *Curiosity's* Instruments

Since landing, *Curiosity* has investigated \sim 680 m of strata using its diverse suite of instruments. Included in the suite are the Mast Camera (Mastcam; Bell et al., 2012) multispectral imager, Chemistry and Camera (ChemCam; Maurice et al., 2012; Wiens et al., 2012) laser, camera, and spectrometer instrument, Chemistry and Mineralogy (CheMin) powder X-ray diffraction and fluorescence instrument (Blake et al., 2012), and Alpha Particle X-ray Spectrometer (APXS; Campbell et al., 2012). Images acquired by the science cameras allow the MSL team to make stratigraphic and textural interpretations; and take quantitative measurements on grain size while spectroscopic data can inform the team of chemical and mineralogic compositions. By synthesizing orbital and in situ data from *Curiosity*, the Sedimentology and Stratigraphy Working Group on the MSL team can define unique stratigraphic units encountered by the rover (Figure 2). After 10 years of exploration and nearly 30 km traveled, *Curiosity's* activities have become relatively conservative in order to preserve the lifetime of rover hardware. Of the rover's instrument suite, Mastcam and ChemCam, both located on the rover mast, are the least time and power intensive and can acquire the most observations at each stop. In contrast, CheMin requires a month's worth of activities, including drilling, and APXS requires arm movement and is often accompanied by the Dust Removal Tool (DRT) to brush dust off the surface. Thus, it is vital to characterize how different surface compositions can be identified in these Mastcam and ChemCam data sets in *Curiosity's* extended mission. In addition to characterizing targets in the rover's immediate workspace, Mastcam can collect multispectral data over broad spatial areas and expand upon stratigraphic units defined from orbit.

1.2. Geologic Context

There are multiple hypotheses for the geologic history of Gale (e.g., Kling et al., 2020; Kraft & Christensen, 2013; Niles & Michalski, 2012) but the data from *Curiosity* are most consistent with lacustrine and aeolian processes



filling and carving the crater interior following the impact (Buz et al., 2017; Rapin et al., 2021). *Curiosity* landed in a relatively flat, lower-elevation region north of Mount Sharp now classified as the Bradbury group. The Bradbury group comprises the oldest and lowest-elevation rocks explored by *Curiosity* (Grotzinger et al., 2015) (Figure 2) and consists of fluvio-deltaic deposits along the crater floor ranging from mudstones to conglomerates (Grotzinger et al., 2015). Stratigraphically above the Bradbury group is the Murray formation of the Mount Sharp group. The origin of the fluvial/lacustrine sediment in the Bradbury Group and Murray formation from streams transporting it down the northern rim of the crater is consistent with orbital and rover observations (Vasavada, 2022). Additionally, Thomson et al. (2019) found that sediments above the elevation of the northern unbreeched rim cannot have been deposited by flowing water. Thus, a significant amount of the sediment in Gale was likely deposited by aeolian suspension. Wind-driven erosion then carved the filled crater into the landscape *Curiosity* is exploring today. In-situ data from *Curiosity* of the Lower Mount Sharp group show laminated mudstones and sandstones which are consistent with lacustrine deposits (Edgar et al., 2020; Fedo et al., 2022; Grotzinger et al., 2015), while strata further up the Mount Sharp group are characterized by a hematite-rich ridge, known as Vera Rubin ridge (VRr). VRr was subjected to early oxidation followed by diagenetic fluids that produced a variety of grain sizes of hematite, and thus colors of the outcrop (Horgan et al., 2020). *Curiosity* then descended VRr but farther up Mount Sharp into a trough-like region known as Glen Torridon, which is particularly enriched in phyllosilicates (Thorpe et al., 2022). In Glen Torridon, the fine-grained mudstones of the Murray formation and the cross-bedded sandstones and laminated mudstones of the Carolyn Shoemaker formation reflect a transition from a low-energy lacustrine depositional setting to fluvial deposits in a lake margin environment (see Section 2.1; Bennett et al., 2023) (Figure 2).

After the Glen Torridon campaign, *Curiosity* traversed through this study's region of interest, the clay-sulfate transition (Figure 1). The clay-sulfate transition comprises the upper Carolyn Shoemaker formation to the Amapari member in the Mirador formation. The Mirador formation is distinguished by cross-stratified sandstone with varying degrees of diagenetic overprinting in Dunnideer and Port Logan members, cross-stratified sandstone with thinly bedded, rippled lenses in the Contigo member (Gupta et al., 2023), and a planar-bedded member (Catrimani) with indeterminate grain size due to strong diagenetic overprints (Figure 2). In the rover's recent exploration of the Mirador formation, it entered "Marker Band Valley," which is surrounded by buttes and comprises the upper ~10 m of the Contigo member, the Catrimani member, and the marker band itself. The dark-toned Amapari marker band displays rippled and rhythmic textures (Gupta et al., 2023; Lewis et al., 2023; Weitz et al., 2023) and a high-Ca pyroxene signature from orbit (Weitz et al., 2022). In-situ analyses by the rover show changes in morphology and chemistry between the sulfate-bearing layers below and above the marker band and the marker band itself (Berger et al., 2023; Gasda et al., 2023; Thompson et al., 2023). Strata in the clay-sulfate transition are hypothesized to represent a transition from a fluvial and lake margin environment to aeolian with wet-dry cycles (Das et al., 2023; Rapin et al., 2023). Unconformably atop Mount Sharp is the Siccar Point Group as a much younger basaltic aeolian sandstone (Banham et al., 2022; Watkins et al., 2022).

CheMin analyses from Glen Torridon reveal phyllosilicates (up to 30 wt.%) such as the dioctahedral smectite nontronite, Ca-sulfates (up to 25 wt.%), hematite (4–8 wt.%), and X-ray amorphous materials (~30–55 wt.%) (Thorpe et al., 2022). The clay-sulfate transition region reveal dioctahedral smectite, with greater abundance at the base of the transition (up to 18 wt.%), hematite (up to 8.4%), goethite (up to 4.1%), Ca-sulfates (up to 20.6 wt.%), starkeyite in one drill target (2.3 wt.%, the first detection of crystalline Mg-sulfate in the Mirador formation), and X-ray amorphous materials (up to 60.9 wt.%) (Rampe et al., 2023). The X-ray amorphous material is primarily made up of the major oxides SiO₂, FeO_T, MgO, CaO, and SO₃, which suggests much of the amorphous component formed via secondary processes (i.e., from water-rock interactions) (Simpson, et al., 2023). CheMin and SAM analyses of the Canaima drill powder from the top of the clay-sulfate transition indicate the presence of amorphous Mg sulfate (e.g., Rampe et al., 2023). These strata and the regional geomorphology suggest that Gale had once been filled with a lake and accompanying sediments via fluvial and aeolian deposition which was then eroded into the modern landscape via fluvial and aeolian processes (Thomson et al., 2019).

The interpretations of clay-sulfate transitions in ancient lacustrine systems on Mars rely primarily on data and analyses of terrestrial analog environments (e.g., Lynch et al., 2015). Clay-bearing strata are characteristic of the following types of deposition on Earth: lacustrine deposits via in situ formation under alkaline or saline conditions if Mg- or Fe- smectites, such as saponite, are major components (Bristow et al., 2009); or continental deposits in soils and weathering profiles caused by alteration of volcanic material if Al- or Fe- phyllosilicates are detected, such as montmorillonite or nontronite (Bristow & Milliken, 2011; Lynch et al., 2015). The detection of Mg-smectites by the Compact Reconnaissance Imaging Spectrometer for Mars (CRISM) instrument on the Mars Reconnaissance Orbiter spacecraft (Murchie et al., 2009), however, does not necessarily confirm a lacustrine deposit. Mg/Fe-smectites, such as saponite and nontronite, may indicate weathering profiles of mafic rocks or hydrothermal alteration due to impacts during early Mars (Bristow & Milliken, 2011). Additionally, these detections are complicated by the fact that these materials have been subjected to erosion and transport over potentially billions of years (Day et al., 2016). Based on closed basin environments studied on Earth (e.g., Currey, 1990; Douglas, 2004), a shift to a drier climate will reduce the water input to the lake thus increasing the concentration of ions and allowing sulfates to form. The abundance of diagenetic features (e.g., nodules, veins, concretions) in Gale crater, however, suggests the possibility of sulfates as a post-depositional diagenetic phase via water-rock interactions (Bennett et al., 2023; Gasda et al., 2022; Rapin et al., 2023; Seeger et al., 2023).

1.3. Motivation

The most phyllosilicate-rich region yet observed, Glen Torridon (Bennett et al., 2023), is overlain by sulfate-bearing strata (Figures 1 and 2). This transition, which was initially identified in orbital data, may indicate a change from a wetter environment that accommodated clay mineral formation to a drier environment that led to the precipitation of sulfates, specifically hydrated Mg-sulfates (Milliken et al., 2010). Mount Sharp is not the only location on Mars where this transition has been observed, which has been hypothesized to signify a global environmental change around the Noachian-Hesperian transition (Bibring et al., 2006).

However, the environmental conditions in which the clay-sulfate transition region formed remain elusive. The multiple working hypotheses include predominantly aeolian depositional settings (Rapin et al., 2019, 2021; Roberts et al., 2023) with some members in Mirador having experienced intermittent diagenetic episodes due to fluvial and/or lacustrine processes (Gupta et al., 2023; Rapin et al., 2023; Seeger et al., 2023). Along with visual analysis of the sedimentology and stratigraphy in rover images, spectroscopy techniques (e.g., APXS, ChemCam, Mastcam) are used to gather chemical data to deduce the complex geologic history of Gale crater. However, diagnostic hydration features of Mg-sulfates in visible to near infrared (VNIR) reflectance spectra are easily masked by the presence of phyllosilicates (Sheppard et al., 2022), further complicating analyses of their history on Mars. Recognizing these challenges, we present a detailed analysis of reflectance spectra from these materials, since understanding the spectral behavior of Mg-sulfates is vital to characterizing the environmental shift in Gale crater's Noachian-aged lake system.

In this study, we use (a) VNIR (447–1,013 nm) multispectral observations from the stereoscopic imaging system, Mastcam, and (b) cross-instrument comparisons with visible (400–840 nm) point spectra from the ChemCam spectrometer, compositional data from the APXS, and X-ray diffraction data from the CheMin instrument to assess the variability of rock spectra in Glen Torridon, Greenheugh pediment of the Stimson formation, and the clay-sulfate transition region including part of Marker Band Valley (MBV) and the rover's first encounter with the

Amapari marker band (Figure 1). We hypothesize that new spectral classes will appear in accordance with new stratigraphic members encountered by *Curiosity* (specifically, we expect the occurrence of absorptions near 1,000 nm in Mastcam spectra due to hydration as *Curiosity* traverses through the clay-sulfate transition). To support mineralogic interpretations of Mastcam spectra of potentially sulfate-bearing targets, we conducted a laboratory investigation of mineral mixtures. Our mixtures consist of Mg-sulfate, phyllosilicates that have been detected by the rover, and crushed Mars-analog basalt to quantify how much Mg-sulfate would be required for Mastcam to detect it. Sheppard et al. (2022) found that a wt.% >10 of montmorillonite can mask the 1.4 and 1.9 μm bands of Mg-sulfate in orbital data. Based on their results, the subtlety of the 1.0 μm band, and the light tone inherent to Mg-sulfates, we hypothesize that it will take small fractions of phyllosilicates and basalt to completely mask the hydration feature around 1.0 μm in spectra convolved to Mastcam wavelengths. The results of this study constrain environmental conditions in which the clay-sulfate transition formed and alteration experienced post-deposition.

2. Background

2.1. Mastcam

Mastcam collects multispectral observations over the VNIR spectral range from 445 to 1,013 nm, providing context for other instruments and broad mineralogic interpretations. Importantly, Mastcam can collect multispectral data over broad spatial areas and expand upon stratigraphic units defined from orbit. The filter positions used by Mastcam makes it sensitive to iron oxides, due to electronic transitions and charge transfers from crystal field theory (Burns, 1993) and some hydrated minerals, due to stretching and bending vibrations (Bishop et al., 2019). Both iron oxides and hydrated minerals are important indicators of alteration (Rice et al., 2013) and thus their identification aids in the reconstruction of Mars' geologic history (e.g., Horgan et al., 2020). In previous work, a database of Mastcam spectra was compiled for *Curiosity*'s traverse from landing through the exploration of VRr (sols 0–2302), from which 9 spectral rock classes were identified (Rice et al., 2022) (Figure 3). Each class has diagnostic spectral features that reflect a mineralogic interpretation and are confined to stratigraphic formations or specific to a geologic feature (e.g., meteorites). In this study we have modified the names of these classes to be more descriptive of either interpreted mineralogy or spectral shape (Figure 3).

Rudolph et al. (2022) synthesized Mastcam multispectral observations across Glen Torridon and found two abundant and widespread spectral types. The first were spectra with strong red slopes and absorption bands centered around 900–950 nm, indicative of Fe-bearing clay minerals in the context of Glen Torridon materials. The second were spectra with strong red slopes and absorption bands centered at 867 nm, indicative of fine-grained, crystalline red hematite. As *Curiosity* continued up Mount Sharp, phyllosilicates disappeared (Rampe et al., 2023) and sulfates became more abundant. Pure epsomite and other polyhydrated Mg-sulfates convolved to Mastcam wavelengths exhibit a “downturn” in the last two wavelength filters as a result of the filter positions and ~950–1,000 nm hydration feature (Figure 4), hereinafter referred to as the R6 downturn. The R6 downturn is characterized by a 1,013/937 nm ratio (R6/R5) < 1.0 but is only diagnostic of hydration if the NIR spectrum is otherwise flat. The R6 downturn has yet to be observed in clay-sulfate transition drill targets. Rather, Mastcam spectra of the tailings (from sols 3055–3612) are characterized by hematite and phyllosilicate abundances (Jacob, 2022).

2.2. Laboratory Investigations of Mastcam's Epsomite Detection Threshold

Multiple studies have proven the ease with which Mg-sulfates dehydrate and rehydrate when exposed to Mars-like pressures and to different relative humidities (RHs) and temperatures (Cloutis et al., 2007; Vaniman et al., 2004). Thus, the identification of Mg-sulfates holds value as an environmental proxy. Vaniman et al. (2004) found that at low pressure and RH, epsomite ($\text{MgSO}_4 \cdot 7\text{H}_2\text{O}$) partially dehydrates and converts to hexahydrite ($\text{MgSO}_4 \cdot 6\text{H}_2\text{O}$). The hexahydrite then becomes amorphous, the rate of desiccation decreases dramatically, and the sample resists complete dehydration. In contrast, the monohydrated phase, kieserite ($\text{MgSO}_4 \cdot \text{H}_2\text{O}$), remains crystalline. When exposed to elevated RH conditions, kieserite easily hydrates and converts to hexahydrite then epsomite. The amorphous material made from hexahydrite recrystallizes to form hexahydrite, pentahydrite ($\text{MgSO}_4 \cdot 5\text{H}_2\text{O}$), and starkeyite ($\text{MgSO}_4 \cdot 4\text{H}_2\text{O}$). Given the results of Vaniman et al. (2004), it is unlikely that Mg-sulfates with high degrees of hydration are stable on Mars; rather, we expect to find Mg-sulfates with intermediate degrees of hydration that are the products of dehydration (Wang et al., 2009, 2016).

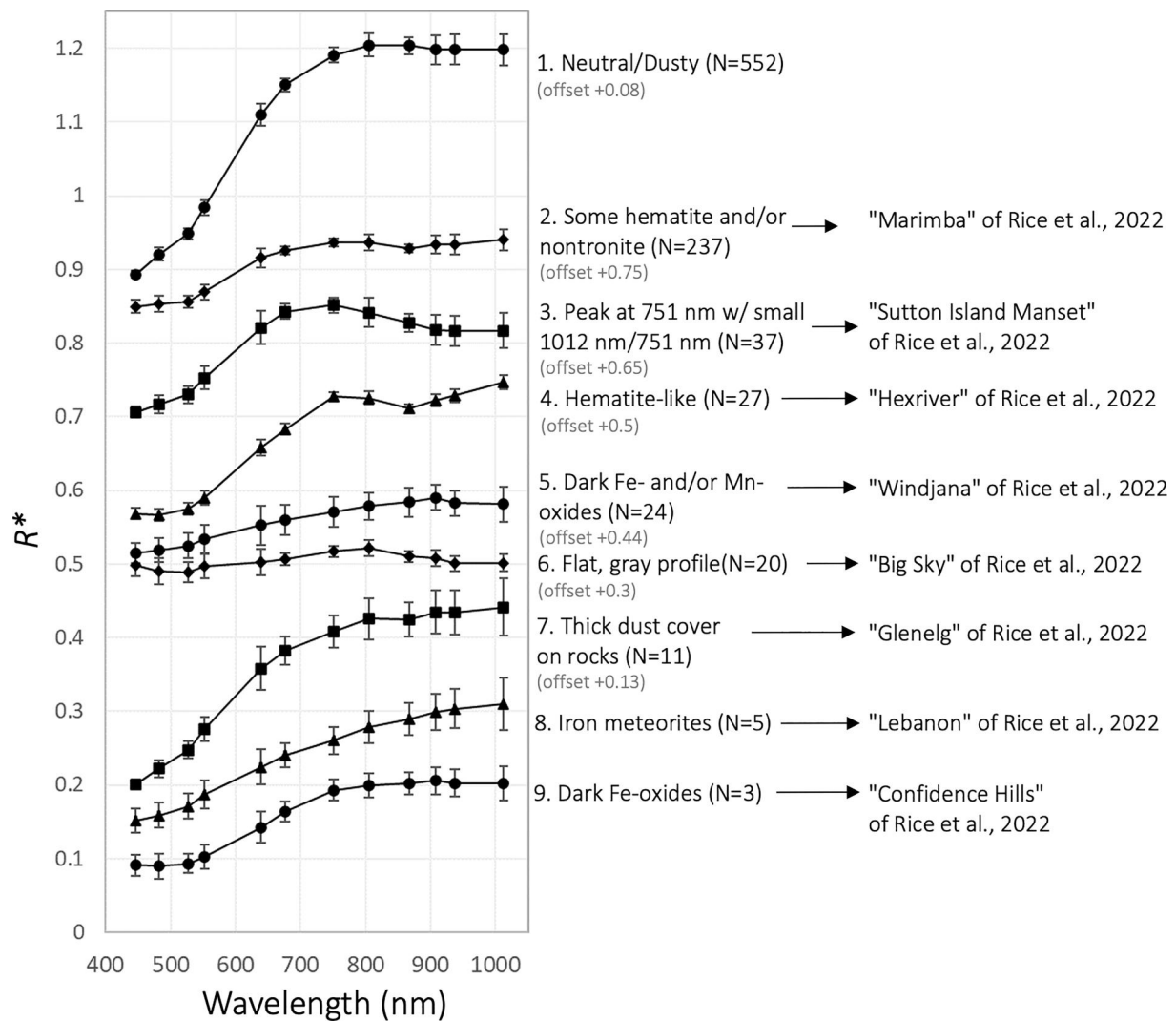


Figure 3. Mastcam rock spectral classes defined by Rice et al. (2022) using observations from landing through Vera Rubin ridge (VRr). Note that the class names have been revised to be more descriptive of either mineralogic interpretation or spectral shape. N represents the number of spectra categorized as this class through VRr. Error bars are the relative standard deviation of each individual spectrum.

Dixon (2018) performed experiments to constrain the amounts of hydrated sulfates that could be detectable using Mastcam bandpasses. They found that mixtures of different Mg-sulfates exhibit more negative slopes at longer wavelengths depending on epsomite abundance, whereas dust-contaminated samples reduced spectral slopes. Examples of species detectable by Mastcam included pure epsomite (at all grain sizes from <63 to $4,000 \mu\text{m}$), and bi-modal mixtures of different Mg-sulfates (epsomite, hexahydrate, and kieserite) with grain sizes of 500 – $1,000 \mu\text{m}$. However, just 5 wt.% of palagonitic dust simulant (JSC-Mars1 at a grain size of $<500 \mu\text{m}$) made epsomite-kieserite mixtures (with ≤ 60 wt.% epsomite) undetectable by Mastcam. Cloutis et al. (2007) found that as time exposed to Mars-like conditions increases, the 1.45 and $1.95 \mu\text{m}$ absorptions in reflectance spectra of polyhydrated Mg-sulfates shallow and the shoulders flatten.

Artificial mixtures of phyllosilicates and sulfates have been used in spectroscopic analysis but were limited to wavelengths outside of Mastcam's spectral range (Sheppard et al., 2022; Stack & Milliken, 2015). In addition, there are scarce studies in which natural materials were included in experimental mineral mixtures (e.g., Roush et al., 2015), which undoubtedly provide valuable information on the spectral behavior of rock and soil targets on Mars. Modeling spectra of mixtures in the NIR has been proven difficult due to the effects of grain size, viewing geometry, and the non-linear mixing behavior (Hapke, 1993; Harris & Grindrod, 2018; Shkuratov et al., 1999), thus warranting lab experiments of multiple mixtures. Most relevant to our lab study are the findings of Sheppard

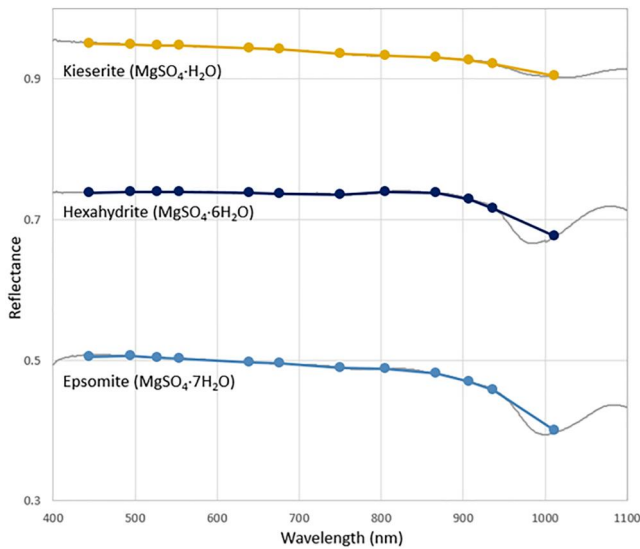


Figure 4. Spectra of synthetic polyhydrated and monohydrated Mg-sulfates convolved to Mastcam wavelengths from Dixon (2018) in color; high resolution spectra in gray. The grain size of these samples is 500–1,000 μm . The small hydration feature around 1,000 nm manifests as an R6 downturn in the last two wavelength filters in convolved spectra (i.e., 1,013/937 nm < 1.0). Band depths decrease with less structurally bound water molecules and smaller grain sizes (Dixon, 2018).

et al. (2022), who found that montmorillonite can spectrally mask the presence of Mg-sulfates if the former is above ~ 10 wt.%. Their analysis, however, was focused on the changes to hydration features outside of Mastcam's wavelength range with applications to CRISM data. Jacob (2022) found in their study of mineral mixtures that the diagnostic R6 downturn of epsomite in Mastcam spectra is easily overwhelmed by plagioclase and pyroxene, even at 50 wt.% epsomite. In this study we quantify the threshold at which the hydration feature around 950–1,000 nm is present in convolved lab spectra of bimodal mixtures of phyllosilicates and epsomite. We also add small fractions of powdered basalt to assess the overall dampening of spectral features.

3. Methods

3.1. Image Analysis and Spectra Classification

Mastcam is a multispectral, stereoscopic imaging instrument with a left (M34) and right (M100) camera. These cameras can acquire VNIR reflectance spectra in 12 unique wavelengths from 445 to 1,012 nm by collecting multiple images through different filters on a spinning wheel. Once through the filter wheel, light travels through a Bayer pattern of broadband RGB filters bonded to a charge coupled device which is used in many digital imaging systems (Bell et al., 2017; Malin et al., 2017). VNIR reflectance spectra are not only sensitive to composition but also to grain size and viewing/illumination geometry. To better understand these effects, Mastcam observations are sometimes acquired multiple times a day under variable solar incidence angles. These types of photometry experiments, and grain size

experiments, are also conducted in laboratories on Earth and can enhance our interpretations of Mastcam multispectral data. In this study, however, Mastcam multispectral observations were restricted to within 1.5 hr of local noon (to limit the calibration uncertainties that arise at high incidence angles and avoid photometric effects). A total of 891 observations acquired with both Mastcam cameras were used, with 266 collected after sol 2302 in Glen Torridon, Greenheugh pediment, and the clay-sulfate transition (Table S1).

For spectral analyses, we followed the methodology described by Rice et al. (2022) and utilize the previously compiled database of observations prior to sol 2302 (Rice, 2022). Raw sensor values were radiometrically calibrated, using a reduction pipeline that included near-simultaneous observations of a calibration target (Bell et al., 2017). Radiometrically calibrated I/F values were converted to reflectance factor (R^*) by dividing by the cosine of the solar incidence angle. To highlight the color and spectral variability, we applied a decorrelation stretch to all calibrated Mastcam images which we used to identify regions of interest (ROIs) representative of the morphologic and color diversity within each scene. Spectra were extracted by averaging the R^* values of pixels within each ROI and compiled in a database with extensive metadata (including feature type, viewing geometry, sol, local true solar time, tau, elevation, L_S , etc.). We followed the “best practices” for identifying and selecting ROIs as described by Rice et al. (2022).

Principal component analysis (PCA) was utilized to understand what spectral features were contributing most to the variability of rock spectra in the data set (sols 2303–3672). We first normalized spectra to 1.0 at their peak reflectance to avoid components related to albedo, especially since non-mineralogic factors can affect overall reflectance (e.g., shadows) (Rice et al., 2022). The average relative standard deviation was restricted to 0–0.2. Eight observations were omitted due to either calibration errors or targets at a distance that could not be correlated with rover elevation. To perform the analysis, we used the Scikit-learn Python package (Pedregosa et al., 2011) and then plotted the resulting PCs against each other to identify spectra that represent the minimum and maximum values of each component.

In order to interpret mineralogic trends across the full data set, we utilized spectro-stratigraphic and parameter plots. The spectro-stratigraphic columns allow for analysis of spectral variations across the traverse as a function of elevation. We selected spectral parameters based on the major spectral contributors to rock spectra, as defined by the PCA. From the clustering of rock spectra within these parameter spaces we identified spectral classes. Some spectral classes are the same as, and others distinct from, the classes of Rice et al. (2022). We used visual

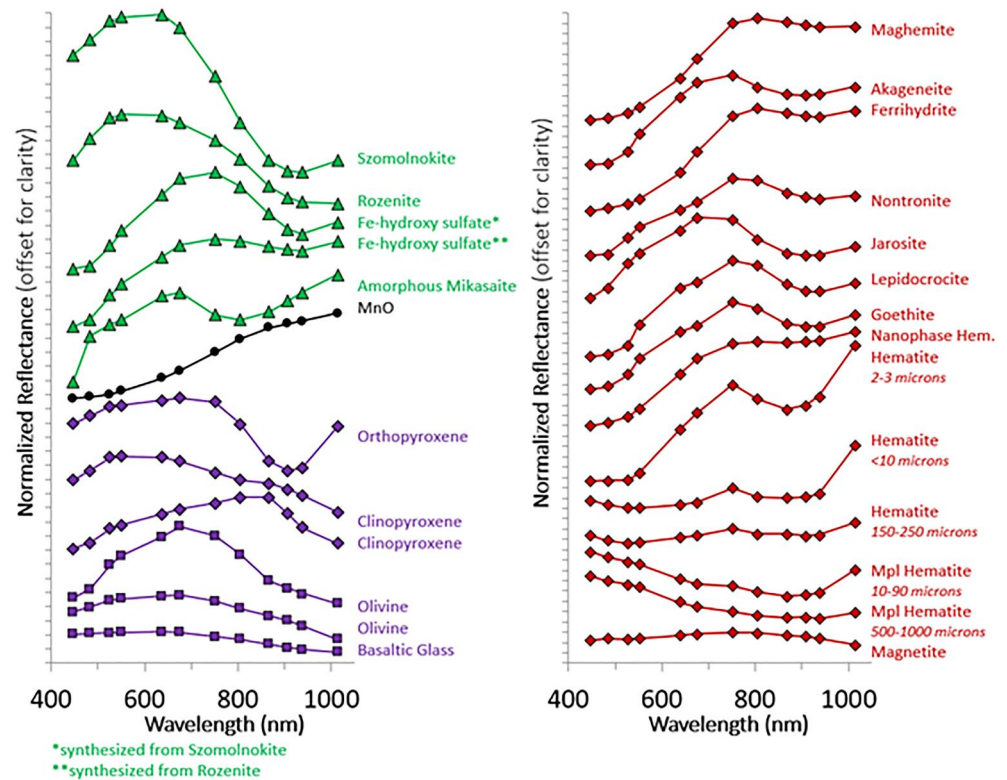


Figure 5. Laboratory spectra of Fe-bearing minerals and oxides, modified from Figure 5 of Rice et al. (2022): ferrous sulfates (light green triangles); MnO (black circles); pyroxenes (purple diamonds); olivines and basaltic glass (purple squares); ferric alteration phases (red diamonds). Ferrous sulfates are from Bishop et al. (2021). The amorphous mikasaite was synthesized by Elizabeth Sklute using the methods described in Sklute et al. (2015). Microplaty (Mpl) hematite spectra are from Lane et al. (2002). Spectra have been convolved to Mastcam spectral bandpasses, normalized to 1.0 at 751 nm, and offset for clarity.

inspection of the parameter plots and the spectra themselves to distinguish unique classes, comparing the Mastcam spectra to spectra of pure minerals from laboratory databases (Figure 5). The spectral parameters that most greatly aided in the analysis and interpretation of Mastcam spectra are summarized in Table 1.

3.2. Cross-Instrument Analyses

Using these new Mastcam spectral classes of rocks, we classified Mastcam spectra of all CheMin target drill tailings to decipher what crystalline minerals are contributing to the shape of Mastcam spectra. The CheMin instrument is an X-ray diffractometer and X-ray fluorescence (XRF) spectrometer that operates in transmission geometry (Blake et al., 2012). CheMin analyzes a few 10 s of milligrams of drill powder or scooped loose sediment, typically over three nights for a total of ~22 hr of analysis. CheMin uses a Co X-ray source to substantially reduce fluorescence from Fe-bearing phases. XRD patterns are collected from 4 to 52°2θ (Co-Kα) with an angular resolution of ~0.3°2θ. Patterns are analyzed via Rietveld refinement (e.g., Rietveld, 1969) and the full-pattern fitting software FULLPAT (e.g., Chipera & Bish, 2002) to quantify mineral abundances to a detection limit of ~1 wt.%, determine unit-cell parameters of minerals present in abundances >5 wt.% of the bulk, and quantify X-ray amorphous abundance.

We also classified all ROI from surfaces subjected to the dust-removal tool (DRT), which mitigates the effects of dust and is utilized whenever possible prior to obtaining APXS rock analyses. In doing so we can compare the Mastcam multispectral classifications of the dust-removed surfaces to elemental abundances. APXS measures the chemistry of rocks, unconsolidated material and the atmosphere on Mars using a combination of particle induced X-ray emission and XRF spectroscopy (see Campbell et al., 2012, 2014, Gellert et al., 2006, 2015; Rieder et al., 2003 for instrument details). APXS acquires elemental abundances for Na, Mg, Al, Si, P, S, Cl, K, Ca, Ti,

Table 1
Summary of Spectral Parameters Used to Characterize Mastcam Spectra

Camera	Parameter	Formula	Possible mineralogic indicators
Left	L6 (1,012 nm)/L3 (751 nm) ratio	$R_{1,012}^*/R_{751}^*$	Used as a proxy for NIR profile; values <1.0 are consistent olivine, clinopyroxene, and basaltic glasses; values >1.05 can be indicative of iron meteorites
Left	L5 (867 nm)/L4 (676 nm) ratio	R_{867}^*/R_{676}^*	Values <1.0 may indicate ferric sulfates or olivine
Left	L1 (527 nm) band depth	$1 - R_{527}^*/(0.645R_{445}^* + 0.355R_{676}^*)$	Larger value can indicate higher degree of Fe oxidation (e.g., Farrand et al., 2008)
Left	L3 (751 nm)/L2 (445 nm) ratio	R_{751}^*/R_{445}^*	Termed “red/blue ratio” and can indicate “redness” of spectra; larger values are consistent with higher degrees of oxidation
Left	L3 (751 nm)/L1 (527 nm) ratio	R_{751}^*/R_{527}^*	A modified version of the “red/blue ratio”; values >1.1 are consistent with iron meteorites (e.g. Wellington et al., 2018)
Left	L5 (867 nm) band depth	$1 - R_{867}^*/(0.556R_{751}^* + 0.444R_{1021}^*)$	Largest values are consistent with presence of fine-grained, red crystalline hematite, and smaller positive values consistent with other Fe-oxides. Negative values indicate a convex NIR profile more consistent with olivine, pyroxenes and nontronite (e.g. Horgan et al., 2020)
Right	1,013/937 nm	$R_{937}^*/R_{1,013}^*$	Used to quantify the spectral “downturn” or “uptick” in the longest Mastcam wavelength. Values >1.0 with otherwise flat NIR profiles are consistent with a hydration band at ~980 nm (Rice et al., 2010). Large values paired with large 805/937 nm ratios are consistent with broader 900–1,000 nm absorptions (e.g., olivines, pyroxenes). Values <1.0 are more consistent with 800–900 nm absorptions (e.g., hematite)

Note. Modified from Rice et al. (2022).

Cr, Mn, Fe, Ni, Zn, and Br, and all elements are normalized to 100% and reported as weight% oxides except for Cl, Ni, Zn, and Br (Campbell et al., 2012; Gellert et al., 2006). Cl is reported as weight% element, and Ni, Zn, and Br as parts per million (ppm). The highest quality APXS data is acquired during cooler temperatures (−25 to −45°C) and over integration times of 4 hr or more. Acceptable quality data can be acquired during as little as 20 min of integration time. The APXS instrument is deployed to contact, or within a 2 cm standoff from the surface to be measured, resulting in a field of view of 1.5–3 cm. Thus, compositional data is acquired from the area within the respective FOV, and from sample depths of 2–5 μm for the lighter elements and 50 μm for the heavier elements (Rieder et al., 2003).

In order to further validate the presence of new classes, we compared Mastcam and ChemCam reflectance measurements from similar surfaces. Relative reflectance data from Mastcam and ChemCam exhibit similar trends in the 400–840 nm region with stratigraphy (e.g., Fraeman et al., 2020; Horgan et al., 2020; Rudolph et al., 2022; Seeger, 2020). As shown by Johnson et al. (2015) ChemCam measurements acquired without the laser on sunlit surfaces have been used as a means of acquiring passive reflected radiance spectra (called “passive spectra”) with absolute calibration uncertainty of ~6%–8%. Relative reflectance spectra in the 400–840 nm region were estimated by dividing a scene radiance spectrum by a white calibration target radiance spectrum, followed by multiplication by the known laboratory reflectance of the calibration target material (e.g., Johnson et al., 2015).

3.3. Laboratory Investigation of Mastcam's Epsomite Detection Threshold

To study the spectra of phyllosilicate-sulfate mixtures, as a comparison to alteration mineral assemblages that Mastcam may encounter, we used a similar suite of minerals to that of Stack and Milliken (2015) and Sheppard et al. (2022), which was based on identifications made previously in CRISM and Observatoire pour la Minéralogie, l'Eau, les Glaces et l'Activité (OMEGA; Bellucci et al., 2004) spectra of Mars. This included the polyhydrated Mg-sulfate, epsomite; smectites, montmorillonite, saponite, and nontronite; and a basalt collected from the Grande Ronde flow of the Columbia River Basalt Group in Eastern Washington State (Figure 6, Table 2). We use epsomite because the Mg-sulfate identified by CheMin, starkeyite, is spectrally similar in the VNIR range but is not stable under typical laboratory conditions. The montmorillonite sample was sourced from the Clay Minerals Society (SWy-1). The saponite sample (SAP101) has been characterized by the University of Winnipeg Planetary Spectrophotometer Facility (UWPSF) with an estimated purity of 98% and minor feldspars. The nontronite sample (NON105 from UWPSF) was collected from the same road cut as the Source Clay Minerals Repository sample SWa-1 in Grant County, WA, USA and has been characterized in detail by Turenne et al. (2023). The

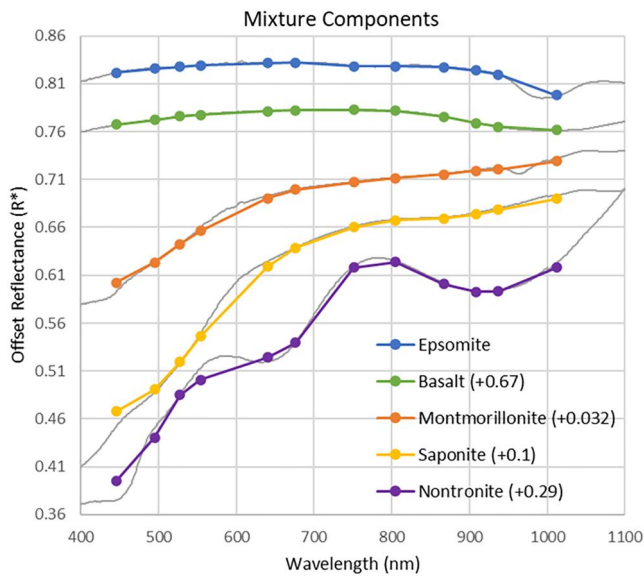


Figure 6. Spectra of mixture components with grain size of 75–106 μm . High-resolution spectra from the Analytical Spectral Devices (ASD) spectrometer shown in gray. ASD spectra convolved to Mastcam wavelengths are shown in color.

Columbia River Basalts have been characterized in detail and proven to be suitable spectroscopic Mars-analogs (e.g., Curtis, 2022; Hoza, 2019; Lapo, 2021; Michalski et al., 2006). None of the trace mineral components in our samples have significant effects on the spectra. Epsomite, nontronite, and saponite were crushed using a mortar and pestle. The basalt was crushed using a mixer mill. All components were dry-sieved to a grain size range of 75–106 μm based on rock grain size measured in situ (e.g., Rivera-Hernández et al., 2020; Minitti et al., 2021). A high precision scale was used to measure the weight of each component in the mixtures.

Spectra were acquired using an Analytical Spectral Devices (ASD) FieldSpec 4 HiRes spectrometer connected to an ASD contact probe which has a fixed geometry of $i = 12^\circ$ and $e = 35^\circ$. Following the methodology of Rice et al. (2010), we convolved each high-resolution laboratory spectrum to the filter bandpasses of Mastcam. These mixtures provided context when defining mineralogic interpretations of spectral classes and characterize the threshold at which Mastcam can detect hydrated Mg-sulfates. Additional high-resolution and convolved reflectance spectra from the UWPSF were also consulted in these analyses.

We started with 10 and 20 wt.% phyllosilicates in the mixtures with epsomite. After assessing the spectra of initial mixtures, we changed the wt.% of the phyllosilicate component to constrain the detection threshold. Small abundances of basalt were then introduced to simulate components of the mudstones in lower Mount Sharp and to assess the resultant dampening of spectral features. The resulting components and their proportions in each mixture are summarized in Table S2 in Supporting Information S1.

4. Results

We use PCA to understand which aspects of the spectra, from Glen Torridon to the rover's first encounter with the Amapari marker band, are contributing the most to the variability of the data set. Once defined, these key spectral parameters correlated to principal components are interpreted as a function of elevation to discern trends with stratigraphy. The resultant spectral variability is used to define new rock spectral classes in the context of spectra from our laboratory mixtures and pure minerals to make mineralogic interpretations (Section 5).

Table 2
Materials Used in Laboratory Mixtures

Material	Formula	Identified in:
Mg-Sulfates		
Epsomite	$\text{MgSO}_4 \cdot 7\text{H}_2\text{O}$	Rapin et al. (2019)
Kieserite	$\text{MgSO}_4 \cdot \text{H}_2\text{O}$	Milliken et al. (2010), Smith et al. (2021), Sheppard, Milliken, et al. (2021), Sheppard, Thorpe, et al. (2021)
Hexahydrite	$\text{MgSO}_4 \cdot 6\text{H}_2\text{O}$	Rapin et al. (2019)
Phyllosilicates		
Nontronite	$\text{Na}_{0.3}\text{Fe}_2(\text{Si,Al})_4\text{O}_{10}(\text{OH})_2 \cdot n\text{H}_2\text{O}$	Milliken et al. (2010), Carter et al. (2015)
Montmorillonite	$(\text{Na,Ca})_{0.33}(\text{Al,Mg})_2(\text{Si}_4\text{O}_{10})(\text{OH})_2 \cdot n\text{H}_2\text{O}$	Carter et al. (2015), Bridges et al. (2015)
Saponite	$\text{Ca}_{0.25}(\text{Mg,Fe})_3(\text{Si,Al})_4\text{O}_{10}(\text{OH})_2 \cdot n(\text{H}_2\text{O})$	Carter et al. (2015), Bristow et al. (2018)
Analogues		
Columbia River Basalts	Plagioclase, pyroxene, ilmenite, apatite, augite, olivine	Michalski et al. (2006), Hoza (2019), Curtis (2022)

Table 3
Principal Components of Rock Spectra With Minimum and Maximum PC Examples in Figures 7 and 8

PC	% variance	Defining spectral characteristics	Max PC examples	Min PC examples
1	76.09	Overall redness (751 nm/445 nm ratio)	Joppa Shore (sol 2472); Edinburgh (sol 2726); Kilmaluag (sol 3209); Calder DRT (sol 3423)	Pitinga DRT (sol 3489); Omai (sol 3504); El Caura (sol 3558); Ilha Novo Destino (sol 3536)
2	16.55	Peak NIR position at 751 versus 908 nm or longward and the 867 nm/751 nm ratio	Edinburgh (sol 2726); Obar Dheathain (sol 2967); Saracura (sol 3643); Tucano (sol 3640)	Maria Gordon dump pile (sol 3247); Parepone (sol 3492); Micobie (sol 3579); Canaima tailings (sol 3613)
3	3.66	527 and 867 nm band depths and the 1,012 nm/908 or 937 nm ratio	Karia Island (sol 3565); Maraca (sol 3635); Shabono (sol 3672); Roxinho (sol 3669)	Videix (sol 3143); Helmsdale Boulder (sol 3248); Linden (sol 3555); El Caura (sol 3558)
4	2.19	Overall NIR slope (1,012 nm/805 nm ratio)	Obar Dheathain (sol 2967); Blis Et Born (sol 3202); El Caura (sol 3558); Arorouta (sol 3553)	Alba Dun Ara (sol 2313); Clyde Gannet (sol 2319); Groken DRT (sol 2907); Lagoa do Paraíso (3544)

4.1. PCA of Mastcam Rock Spectra

In PCA of rocks in Glen Torridon and the clay-sulfate transition, 76.09% of the variance lies in PC1, 16.55% in PC2, 3.66% in PC3, and 2.19% in PC4, and 1.50% in remaining components (Table 3). PC1 versus PC2 is plotted in Figure 7, with each point representing a rock spectrum color-coded by stratigraphic member and the Amapari Marker Band. By inspecting spectra that are characterized by minimum and maximum PC values, we can identify which spectral features are contributing to the variability of the data set. Examples of spectra with minimum and maximum component values are displayed in Figure 8. PC1 corresponds to the overall “redness” of rock spectra which can be quantified by the L3/L2 (751 nm/445 nm) ratio. The “redness” of rock surfaces—which can correlate with ferric components and/or dust cover—is the major control on spectral shape for rocks at all Mars landing sites, as shown in PCA results from the Mars Exploration Rover (MER) Pancams (e.g., Farrand et al., 2008), *Curiosity's* Mastcam in the early traverse (Rice, 2022) and *Perseverance's* Mastcam-Z (Rice et al., 2023). PC2 is characterized by two spectral features: the peak NIR position and the 867/751 nm ratio (Figure 8). The 867/751 nm ratio has previously been shown to correlate with phyllosilicate abundance in some instances (Jacob, 2022). The features that correlate with PC2 had not been a large contributor to the variability of Mastcam spectra from *Curiosity's* earlier traverse (Rice et al., 2022); we use this component, in part, to define a new spectral class (see Section 5). PC3 corresponds to the 527 and 867 nm band depths and the 1,012/908 nm or 1,013/937 nm ratio. The latter did not significantly contribute to the variability of rock spectra in *Curiosity's* earlier traverse (Rice et al., 2022). PC4 is characterized by the 1,012/805 nm ratio.

Geologic formations in the clay-sulfate transition, specifically the Mirador formation, show greater amounts of spectra characterized by minimum PC2 compared to those in Glen Torridon (Figure 7). PC3 also contributes significantly to the spectral variability of the Mirador formation (Figure 7). Additionally, spectra from the Stimson formation and Amapari Marker Band are markedly characterized by smaller PC3 values (Figures 7 and 8). The Murray formation in Glen Torridon is characterized by minimum PC4 values (Figure 7).

4.2. Trends With Elevation, Stratigraphy, and Dust Cover

In order to assess spectral trends with stratigraphy, we analyzed key spectral features as a function of rover elevation. A larger percentage (67.27%) of rocks in the Mirador formation have 1,013/937 nm ratios <1.0 in comparison to the rest of the traverse (Figure 9). Like spectra of rocks in the Murray formation, DRT targets don't have substantially different 1,013/937 nm ratios compared to dusty rocks. The dust-cleared targets and dusty counterparts between −3,980 and −3,960 m with 1,013/937 nm ratios <~−0.96 are from Greenheugh pediment. Like in the Jura member of the upper Murray, the 527 nm band depths in spectra of rocks in Glen Torridon do not exhibit clear relationships with dust-cleared rocks (Figure 9). In the clay-sulfate transition, the 527 nm band depths in spectra of rocks from upper Pontours to Contigo slightly increases in dust-cleared rocks, similar to that of Pettegrove Point in the upper Murray. Few rock spectra from Glen Torridon and clay-sulfate transition have 867 nm band depths >0.05 overall; and few dusty rocks have 867 nm band depths >0 compared to VRr in the upper Murray formation. In rock spectra

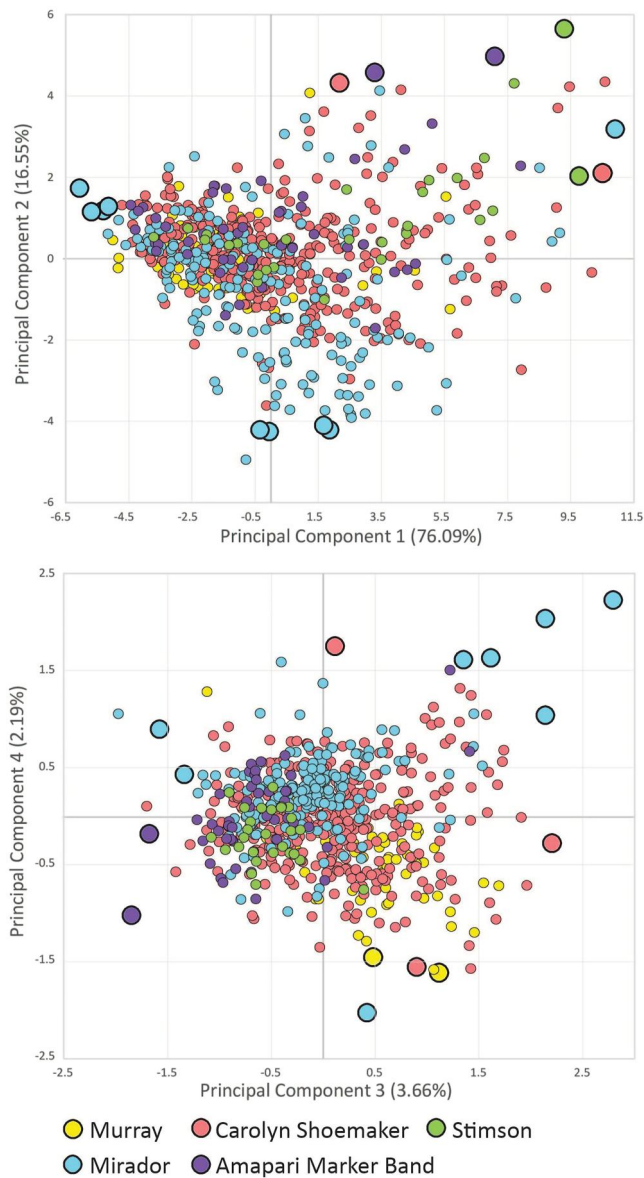


Figure 7. Principal component analysis results for all rock spectra in Glen Torridon and clay-sulfate transition. Points are color-coded by formation. Larger circles indicate the minimum and maximum PC example spectra shown in Figure 8.

mixtures produces convex NIR profiles with the most basalt-like spectrum being the 80/20 mixture with 10 wt.% basalt.

5. Discussion

5.1. New Rock Spectral Classes

Using a combination of PCA (Section 4.1) and analyses of spectral trends with stratigraphy (Section 4.2), we propose four new rock spectral classes that characterize Glen torridon, Greenheugh pediment, and the clay-sulfate transition (Figure 13, Table 4); we refer to these as Classes J-M, with Classes A-I referring to those previously defined by Rice et al. (2022).

from the clay-sulfate transition, the effect of dust on the 867 nm band is drastically reduced by the DRT and in drill tailings in comparison to the rest of the traverse (Figure 9). The 867 nm band depths in spectra of dust cleared targets in Catrimani and Amapari exhibit smaller values than the rest of the Mirador formation.

4.3. Laboratory Spectra

4.3.1. Epsomite and Montmorillonite

In a two-phase mixture of epsomite and montmorillonite, we find that the minimum wt.% epsomite needed to produce the R6 downturn (1,013/937 nm ratio <1.0) characteristic of the hydration in epsomite is 90 wt.%, which is consistent with the findings of Sheppard et al. (2022) (Figure 10). With the addition of 5 wt.% basalt, the 1,012/937 nm ratio approaches 1.0. The 1,012/937 nm ratio in the epsomite-montmorillonite mixtures exceeds 1.0 at 20 wt.% montmorillonite. In mixtures with epsomite-montmorillonite ratios 90/10 and 80/20, the 1,012/937 nm ratio >1.0 is eradicated by 10 wt.% basalt powder. Key spectral features of pure basalt (e.g., broad pyroxene absorption due to Fe²⁺ longward of 1,012 nm) are present in all mixtures with 10 wt.% basalt powder but are most prominent in the 80/20 epsomite-montmorillonite mixture with 10 wt.% basalt.

4.3.2. Epsomite and Nontronite

In a two-phase mixture of epsomite and nontronite, the 1,012/937 nm ratio in the spectra convolved to Mastcam wavelengths is >1.0 in all mixtures (Figure 11). The most notable change with increasing nontronite wt.% is the increase of the 900 nm band depth and the 751/527 nm ratio, increasingly negative 527 nm band depths, and the overall change in reflectance (i.e., spectra are flatter with more epsomite). The lower the wt.% nontronite in the two-phase mixtures, the stronger the effect that the basalt powder addition has on the spectra. In the 90/10 and 80/20 epsomite-nontronite mixtures with basalt powder additions, increasing basalt wt.% shifts the 900 nm band center to 937 nm.

4.3.3. Epsomite and Saponite

In a two-phase mixture of epsomite and saponite, there is a small 1,012/937 nm ratio in the spectra convolved to Mastcam wavelengths in the mixture with 5 wt.% saponite (Figure 12). As wt.% saponite increases, the overall slope reddens and the 1,012/937 nm ratio increases. In the 95/05 and 90/10 epsomite-saponite mixtures, increasing the basalt wt.% flattens the NIR slope. Increasing the basalt wt.% in the 80/20 epsomite-saponite

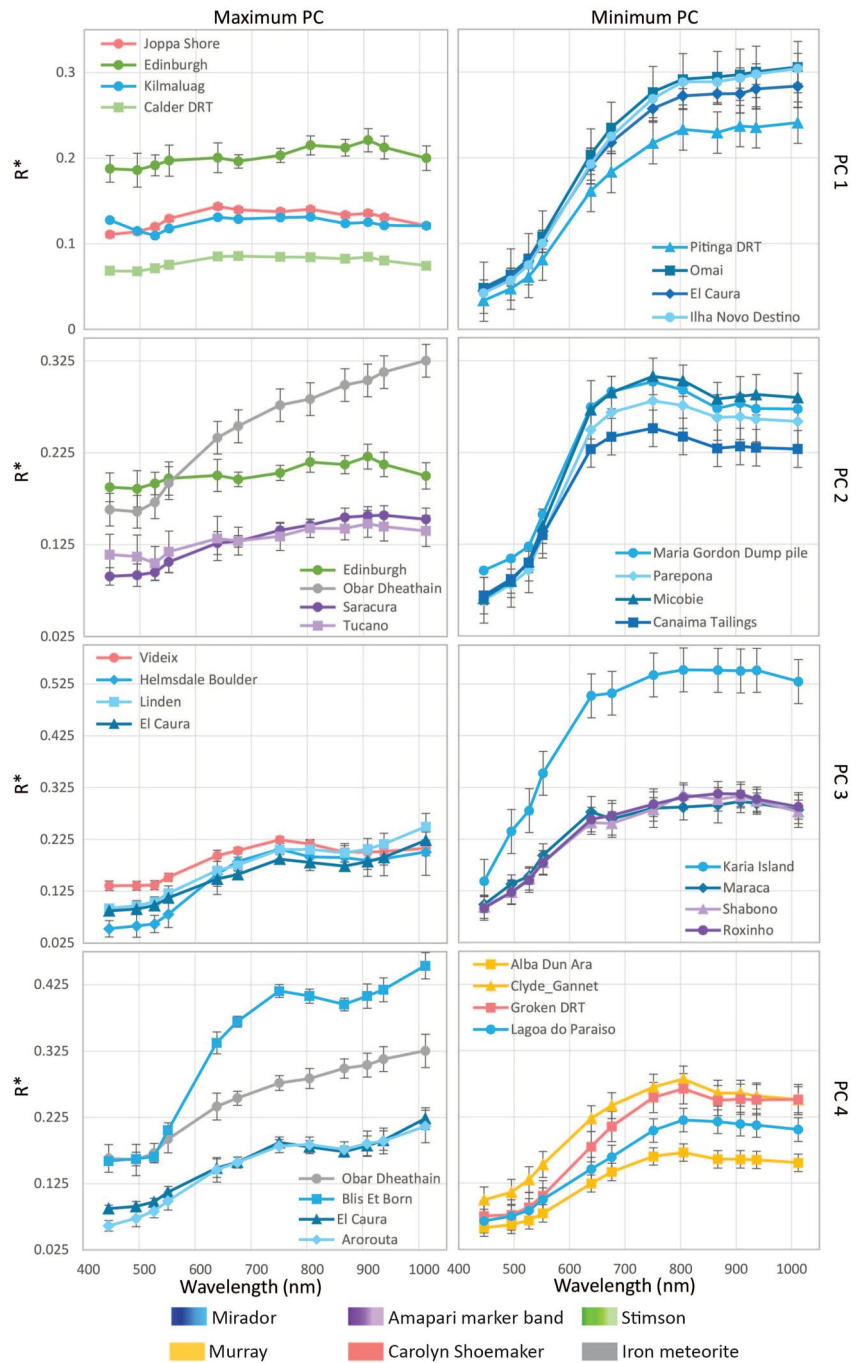


Figure 8. Example spectra for minimum and maximum PC values which correspond to the large points in Figure 7. Each row represents a different principal component, which is labeled to the right of the plots. Spectra are color-coded by stratigraphic formations, the Amapari marker band, and iron meteorites.

Class J (“Red VIS slope with small 1,013/937 nm ratio” class; Figure 13) is characterized by positive slopes in visible wavelengths, like Class A, but with a distinct R6 downturn in the last two wavelength filters, potentially indicative of hydration (Rice et al., 2010). If the 1,013/937 nm ratio is less than 1.0, it is only included in the class description if it does not appear to be a continuation of a negative slope from 867 nm (i.e., it is indicative of hydration and not a broader absorption due to iron). Class K displays negative slopes from 639–751 to 1,012 nm and positive 527 nm band depths. Class L (“Convex profile with small 1,012/867 nm ratio” class) displays a shallower red VIS slope in comparison to classes A and J, with a very small positive slope from 639 to 867 nm and

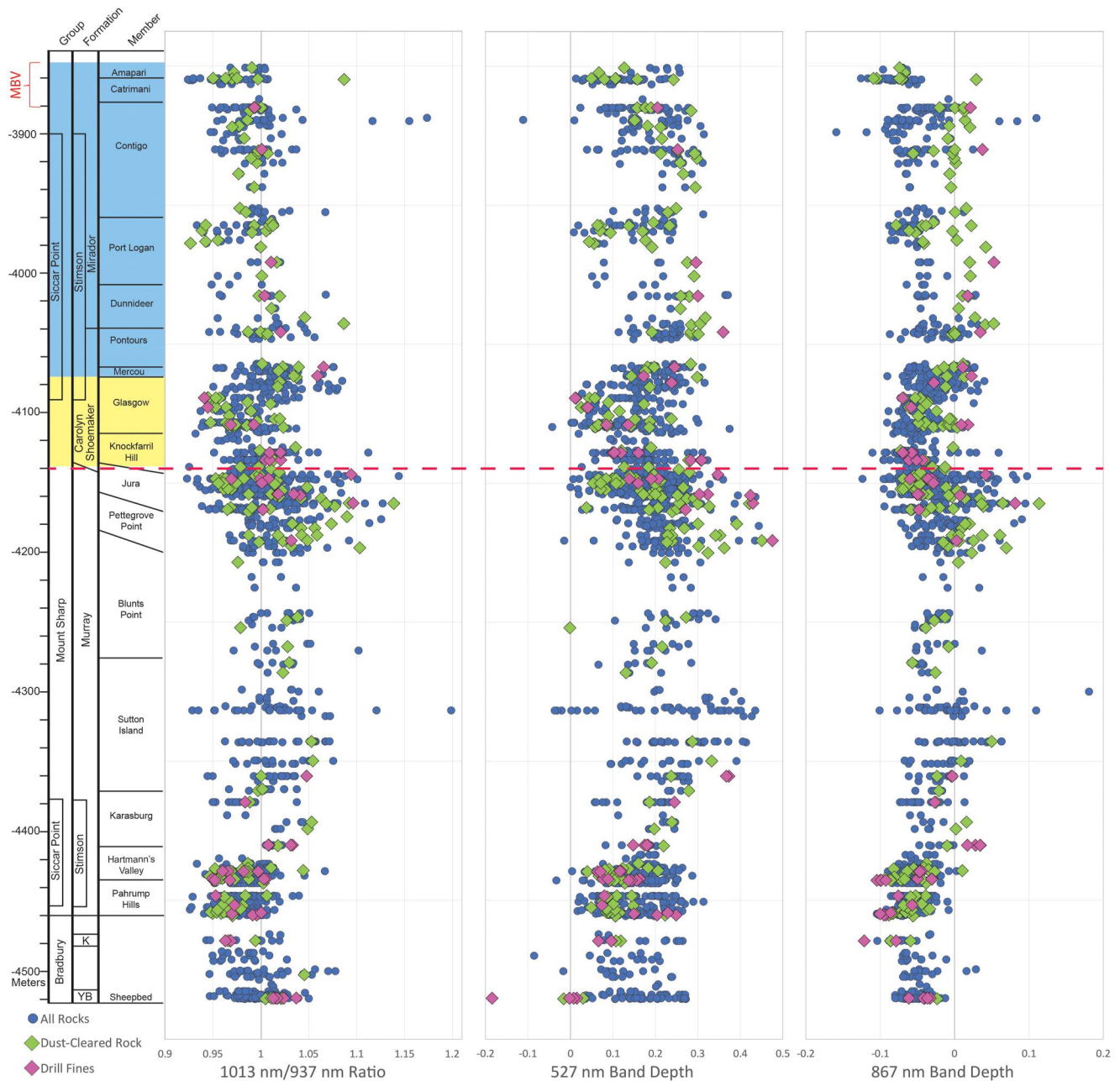


Figure 9. Spectral variability across *Curiosity*'s traverse, for dust-cleared rocks (Dust Removal Tool targets, green diamonds), drill fines (pink diamonds) and all other rock targets (blue dots). MBV = Marker Band Valley. Left: 1,013 nm/937 nm ratio. Middle: 526 nm band depth. Right: 867 nm band depth. Points below red dashed line are observations synthesized by Rice et al. (2022); those above the red dashed line are from this study.

a small 1,012/867 nm ratio. Class M (“Flat profile with small 1,013/937 nm ratio” class) displays some of the flattest spectral profiles of rocks across the entire traverse with a small 1,013/937 nm ratio and in many cases, a very small 867 nm band depth.

The parameters that best distinguish the new classes from each other (and previously established classes) are the 1,013/937 and 867/676 nm ratios (Figure 14). A greater percentage of rock spectra from clay-sulfate transition have 1,013/937 nm ratios <1.0 in comparison to the rest of the traverse (Figures 9 and 14), which is consistent with PC3. The 867/676 nm ratio characterizes the spectral shape between these two wavelengths and is also a variation on PC2. Parameters concerned with shorter wavelength features do show variations but do not appear to be as useful for distinguishing like-spectra from the rest of the data set.

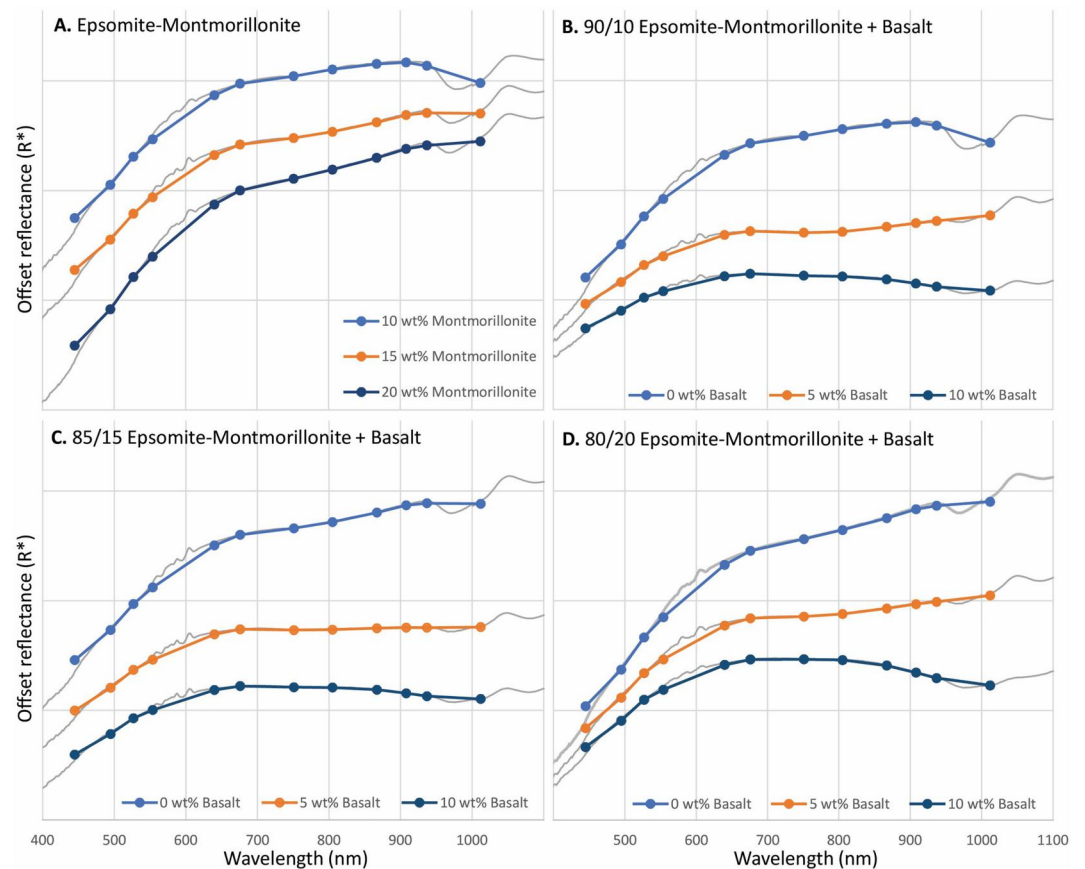


Figure 10. Epsomite-montmorillonite mixtures in (a) with 5 and 10 wt.% basalt additions in (b–d). Gray lines are high-resolution spectra from the Analytical Spectral Devices (ASD) spectrometer. Blue, orange, and dark blue points represent the ASD spectra convolved to Mastcam bandpasses. Reflectance is offset for clarity and all Y-axes scales are equal. The “wobbles” between 552 and 639 nm are a result of a known instrument artifact due to the order-sorting filters in the ASD spectrometer. The R6 downturn due to epsomite is only present in the mixture with 90 wt.% epsomite and 10 wt.% montmorillonite.

5.2. Distributions of Classes With Stratigraphy

We find notable distributions of pre-established and new classes throughout Glen Torridon, Greeneheugh pediment, and the clay-sulfate transition. Glen Torridon is primarily characterized by Class B with some occurrences of Class C, D, F, G, and K (Figures 15 and 16). The Glasgow member in Glen Torridon is marked by the occurrence of Classes D and K; both of which signify alteration and are consistent with the findings of diagenesis in the Glasgow member (Bennett et al., 2023; Rudolph et al., 2022). Above Glasgow and Glen Torridon, Class J appears in accordance with significantly dusty rocks on and around Mount Mercou (Figure 16). The occurrence of Class B persists through the clay-sulfate transition, but along with it the abundance of Classes C and K increases (Figure 16). Classes K and C occur in clay-sulfate transition more than Glen Torridon (Figures 15c, 15e, and 16) and can be correlated to higher abundances of nodules, dark-toned fins, and diagenetic overprints (Figure 17) (Rice et al., 2022). Class M directly corresponds to the rover’s excursions onto Greeneheugh pediment, which is a part of the Stimson formation, and float rocks leading up to the pediment (Figure 15). One exception is the Hutton drill just below the Carolyn Shoemaker formation/Stimson unconformity in a relatively lighter-toned area (Thorpe et al., 2022). Class M spectra are typically of smooth, dust-removed, dark gray surfaces (Figure 17).

Moving up section into MBV, we see the occurrence of Classes C and K persist in accordance with diagenetic features. In the marker band itself, two new spectral classes appear. Spectra classified as J are from the lower rippled and upper rhythmic units of the Amapari marker band and its respective rippled floats just below (Figures 15f and 16). Class J spectra are from primarily dusty, eroded surfaces on the Amapari marker band (Figure 17). Similar to Class J, Class L only occurs within the Amapari marker band or its respective float rocks

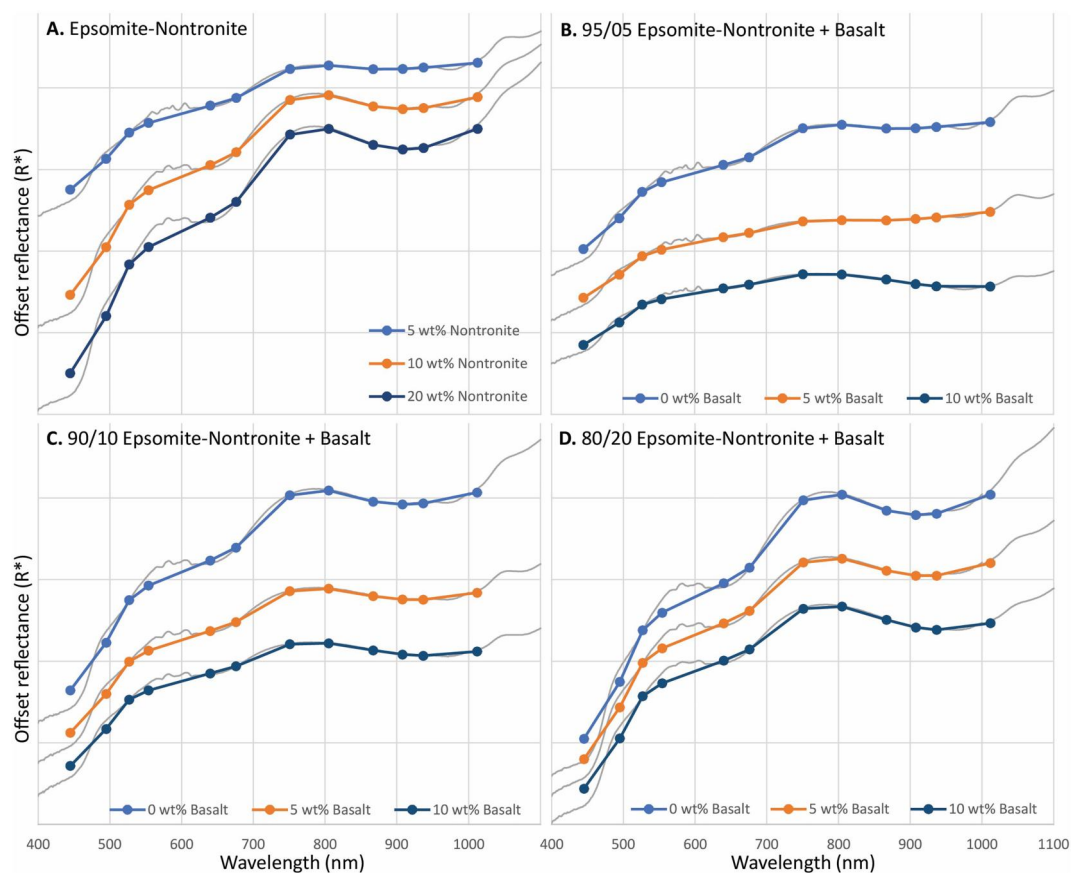


Figure 11. Epsomite-nontronite mixtures in (a) with 5 and 10 wt.% basalt additions in (b–d). Gray lines are high-resolution spectra from the Analytical Spectral Devices (ASD) spectrometer. Blue, orange, and dark blue points represent the ASD spectra convolved to Mastcam bandpasses. Reflectance is offset for clarity and all Y-axis scales are equal. The “wobbles” between 552 and 639 nm are a result of a known instrument artifact due to the order-sorting filters in the ASD spectrometer. The R6 downturn due to epsomite is not present in any of the mixtures with nontronite.

(Figures 15f and 16). Class L spectra are from targets with slightly lighter-toned and relatively matte surfaces from the rippled unit of the Amapari marker band (Figure 17). Class E occurs in accordance with the dark, shiny surfaces on the rippled unit of the Amapari marker band, which is consistent with its pre-established mineralogic interpretation and ChemCam and APXS results of higher MnO and FeO abundances (Gasda et al., 2023; Weitz et al., 2023) (Figure 16).

5.3. Comparisons to Lab Spectra and Mineralogic Interpretations

In order to make mineralogic interpretations of the newly defined classes, we consult laboratory spectra of pure minerals and the mixtures analyzed in this study. Specifically, we take Mastcam-convolved spectra of pure minerals and plot them using the same parameters described above to understand how the pure minerals influence the spectral features that characterize the classes (Figure 18). If a pure mineral plots in or around a spectral class' parameter space, it can indicate if it is a possible contributor to the spectral shape.

5.3.1. Class J

Of the candidate mineral contributors, Ca-pyroxenes and epsomite could explain the location of Class J in this parameter space (Figure 18). Class J is localized to the marker band, where detections of high-Ca pyroxenes have been made from orbit, and occurs on primarily dusty surfaces (Weitz et al., 2022; see Section 5.1). However, laboratory experiments have shown that it is unlikely that a mixture of ferric dust and pyroxenes would result in small enough 1,013/937 nm ratios to reproduce the R6 downturn that defines Class J (Clouits et al., 2000). Evidence from other instruments for lack of sulfates in the majority of marker band targets (Gasda et al., 2023;

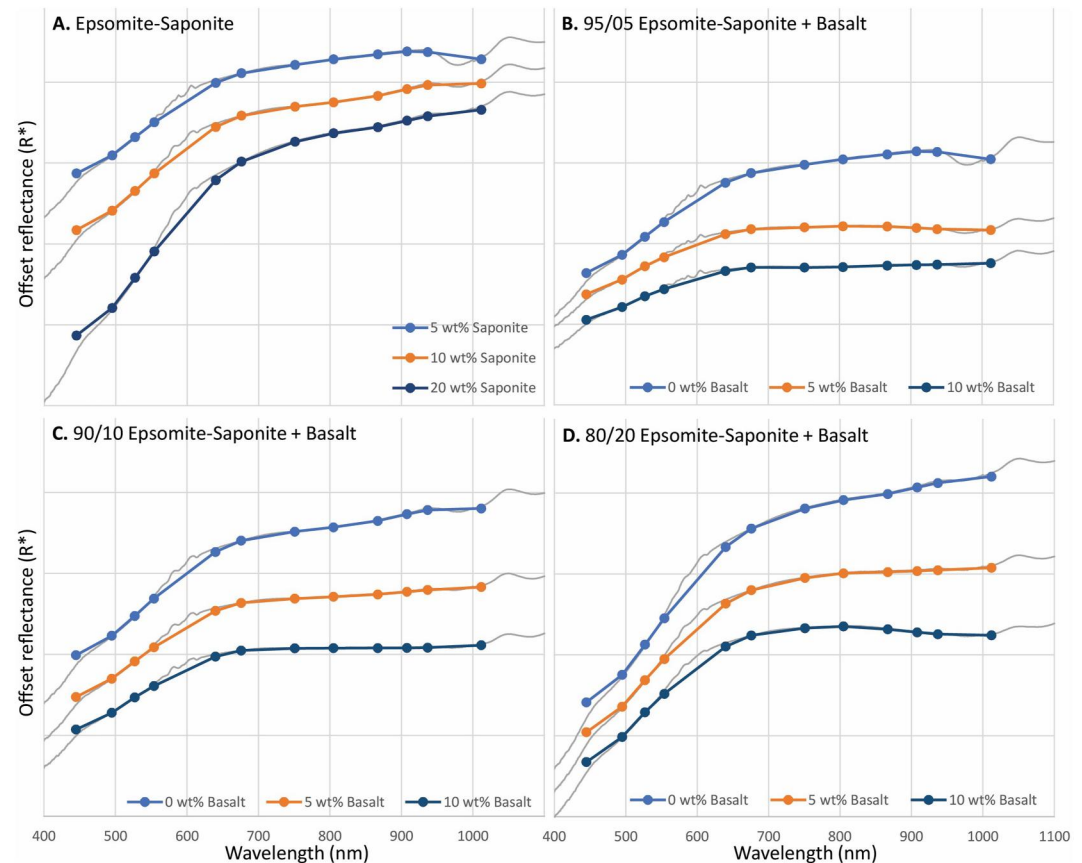


Figure 12. Epsomite-saponite mixtures in (a) with 5 and 10 wt.% basalt additions in (b–d). Gray lines are high-resolution spectra from the Analytical Spectral Devices (ASD) spectrometer. Blue, orange, and dark blue points represent the ASD spectra convolved to Mastcam bandpasses. Reflectance is offset for clarity and all Y-axis scales are equal. The “wobbles” between 552 and 639 nm are a result of a known instrument artifact due to the order-sorting filters in the ASD spectrometer. The R6 downturn due to epsomite is only present in the mixture with 95 wt.% epsomite and 5 wt.% saponite.

Weitz et al., 2023), and the results of our laboratory mixtures, support that the R6 downturn in Class J is not due to hydrated Mg-sulfate. Furthermore, DRT targets in the marker band don't have substantially different 1,013/937 nm ratios compared to dusty rocks (Figure 9) which implies that the ratio cannot be attributed to Mg-sulfate or an underlying material. Spectra similar to those Class of J from MER Spirit's Pancam (Johnson et al., 2021; Rice et al., 2010) and Perseverance's Mastcam-Z (Rice et al., 2023) have been noted on dust-coated rock surfaces and are attributed to hydration in dust at certain viewing geometries; we propose that this explanation is reasonable for the Class J spectra here as well.

5.3.2. Class K

A primary ferrous mineral (e.g., olivine, pyroxene) and/or basaltic glasses are consistent with the shape of Class K (Haber et al., 2022) (Figures 5 and 18). Given that the diagenetic features inherent to Class K are Mg-sulfate-rich (Gasda et al., 2023); and the dust-removed APXS targets classified as Class K exhibit relatively low FeO abundances, it is more likely that a basaltic component influences—but is not the sole contributor to—the reflectance spectra. A minor basaltic component of Class K is further supported by our laboratory mixtures in which just 5–10 wt.% basalt powder reduces the NIR slope when added to two-phase mixtures of epsomite and phyllosilicate (See Section 4.3). The only other stratigraphic members in which Class K has been identified are the sulfate-enriched Sutton Island (Haber et al., 2022) and the diagenetically altered Glasgow (Rudolph et al., 2022), implying that a unique secondary phase may be contributing to the spectral shape. Furthermore, Class K is primarily associated with diagenetic features in the clay-sulfate transition where rocks have large fractions of amorphous sulfur-bearing phases that are likely mixtures of Mg-, Fe-, and possibly Ca-sulfates or sulfites (Gasda

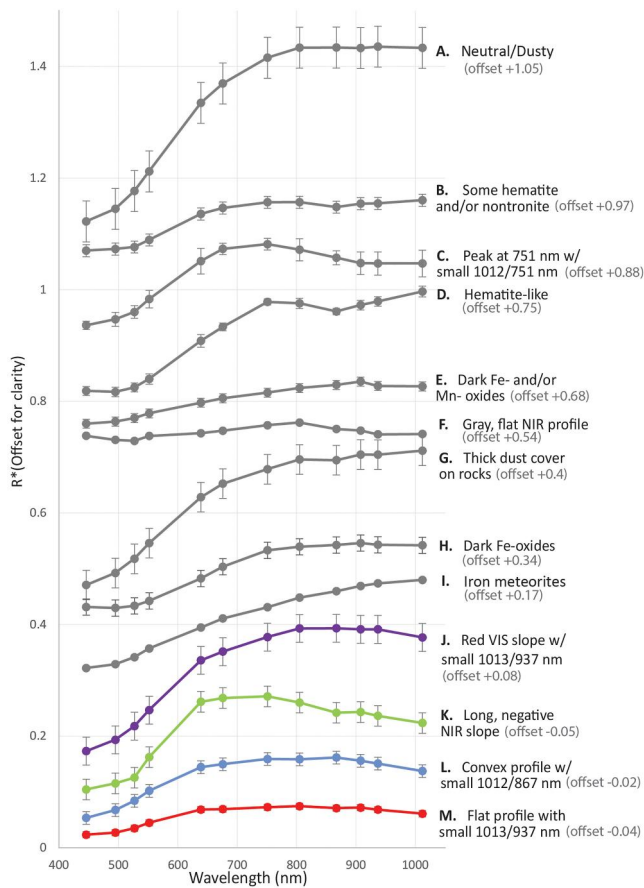


Figure 13. Example spectra of pre-established classes (A–I in gray) from *Curiosity*'s traverse from landing through Vera Rubin Ridge (Rice et al., 2022); and newly defined classes (J–M in purple, green, blue, red) from *Curiosity*'s traverse from Glen Torridon to the Amapari marker band.

graphic distribution), Class C may be characterized by a larger amount of hematite, nontronite, or amorphous ferric sulfates, which are consistent with larger 1,012/751 nm ratios (Figure 18b) (Sklute et al., 2015). Thus, given the disappearance of phyllosilicates in CheMin data starting at the Maria Gordon (MG) target (sol 3226), Class K may be characterized by a primary ferrous component with: (a) coarse-grained ferric oxides (e.g., goethite and hematite), and an amorphous Fe-sulfate component post sol 3226; and (b) nontronite, hematite, and an amorphous Fe-sulfate component pre sol 3226. Furthermore, Class K resembles the “Newberry” class inherent to spherules in the Matijevic formation encountered by the Opportunity rover and identified by Farrand et al. (2014); both interpretations of these classes are consistent with a ferric mineral component.

5.3.3. Class L and M

Several factors support a mineralogic interpretation of Ca-rich pyroxene for Class L. First, Class L is only found in the pyroxene-rich Amapari Marker Band (see Section 5.2.3; Weitz et al., 2023). Second, the 1,012/867 nm ratios <1.0 is consistent with the shape of Ca-rich pyroxene. Lastly, the region in parameter space associated with Class L is characterized by the position of Ca-rich pyroxenes, augite and diopside. Class M spectra are consistent with olivine, magnetite and possibly microplaty hematite (Figure 18). The locations, surfaces, and compositions of Class M support a primarily basaltic component with increased alkalis (See Sections 5.5) and low Chemical Index of Alteration (CIA, Dehouck et al., 2022), which is consistent with the lack of Fe³⁺ absorptions in Class M spectra (Rudolph et al., 2022). Like for Class J, the laboratory mixtures described here and by others (Jacob, 2022)—in addition to results from other *Curiosity* instruments (see Sections 5.4 and 5.5 below)—support the interpretation that the 1,013/937 nm < 1.0 in Class M is not due to hydrated Mg-sulfate. Instead, the 1,013/

et al., 2023; Smith et al., 2022). Thus, considering crystalline Fe-sulfate was not detected by CheMin in the clay-sulfate transition, we investigate the influence an amorphous Fe-sulfate component may have on the spectra.

Using the Sample Analysis at Mars instrument Evolved Gas Analysis, Clark et al. (2023), found that all seven drill samples in the clay-sulfate transition evolved broad SO₂ releases consistent with Fe-sulfates, which either occurred in the amorphous component or were present in abundances lower than CheMin's detection limit. If contributing to Class K, a ferric sulfate present in the amorphous component would need to be in amounts small enough to preserve the negative NIR slope, considering the positive NIR slope inherent to most amorphous phases (Sklute et al., 2015). Alternatively, there could be a relatively larger amount of an amorphous ferrous or Fe-hydroxy sulfate contributing to the shape of Class K—both of which are consistent with negative NIR slopes or 1,012/751 nm ratios <1.0 (Bishop et al., 2021; Sklute et al., 2015) (Figures 5 and 18). Furthermore, VNIR spectra of an amorphous ferric sulfate precipitated onto a flood basalt produced longer negative NIR slopes in comparison to the uncoated sample (Sklute et al., 2015), which we propose is consistent with Class K.

The addition of an Fe-sulfate phase alone would not produce the 527 nm bands in many spectra defined as Class K. Thus, potential ferric iron-bearing minerals that could contribute to the 527 nm bands in Class K, while preserving the negative slope from 676 or 751–1,013 nm, include nontronite, goethite (Cloutis et al., 2006), magnetite, and/or small amounts of hematite (Figures 5 and 18b). With increasing grain size, nontronite and goethite Fe³⁺ spin forbidden absorptions around 900 nm shift right and/or broaden (Turner et al., 2023; UWPSF), which in turn reduces the NIR slope in convolved Mastcam spectra and is consistent with Class K. In our nontronite-epsomite mixtures, the positive slope of the right shoulder inherent to an Fe³⁺ absorption (1,012/867 nm ratio) approaches 1.0 with increasing epsomite and basalt abundances, which may reflect the shape of Class C that we found to correlate with Mg-sulfate strata in our APXS investigation (see Section 5.5). Considering Class K's relationship to Class C (similar surfaces and strati-

Table 4
Summary of Rock Spectral Classes (Rice et al., 2022) With New Classes Marked by an Asterisk

Class	Defining spectral characteristics	Type examples	Distribution	Interpretation
A. Neutral/Dusty	Moderate 751/445 nm ratios; Small values of 1,012/751 nm ratio; Flat NIR profiles	sol 183, mcam00993	Consistent throughout the traverse	Variable amounts of dust upon rocks with neutral spectra
B. Some hematite and/or nontronite	Large 751/445 nm ratios; Small values of 1,012/751 nm ratio; Positive 867 nm band depths	sol 1425, mcam07034	Prevalent in the Murray, Carolyn Shoemaker, and Mirador formations	Rocks bearing some red hematite and/or nontronite
C. Peak at 751 nm with small 1,012 nm/751 nm ratio	Peak reflectance at 751 nm; Small 1,012/751 nm ratios; Positive 867 nm band depths	sol 1524, mcam0770	Primarily within the Sutton Island member and the clay-sulfate transition	Dark, diagenetic features, possibly nontronite-bearing
D. Hematite-like	Large 867 and 527 nm band depths	sol 1885, mcam09853	Mostly within the Sutton Island and Jura members, with significant local variability	Strongly diagenetically altered rocks containing red hematite, nontronite and/or ferric phases
E. Dark Fe- and/or Mn- oxides	Straight, flat to positively sloping profiles to 908 nm; 908/1,013 nm <1.0	sol 626, mcam02676	Primarily within the Kimberley formation, Pahrump Hills member, and the Amapari marker band	Rocks with variable contributions of dark Fe- and/or Mn-oxides
F. Gray, flat profile	1,012 nm/751 nm ratios close to 1.0; blue/red ratios positive or close to 1.0; often has a small 527 nm >1.0 and peak at 805 nm	sol 1120, mcam04990	Drill fines, mostly within the Stimson formation	Rock interiors with minimal spectrally neutral phases (e.g., crystalline SiO ₂ , magnetite)
G. Thick dust cover on rocks	Large 751/445 nm ratios; Positive 1,012/751 nm ratios; no 867 nm band depth	sol 069, mcam00486	Seen within Bradbury Group and clay-sulfate transition	Thick dust cover on rock surfaces
H. Iron meteorites	1,012/751 nm ratios >1.1; 741/527 nm ratios 1.0–2.0	sol 640, mcam02718	Isolated float rocks, found sporadically at all elevations	Iron meteorites
I. Dark Fe-oxides	Large 527 nm band depth; flat NIR profile	sol 758, mcam03257	Only seen within Pahrump Hills member	Dark Fe-oxide, possibly coarse-grained hematite
J. Red VIS slope with small 1,013/937 nm ratio*	Neutral/Dusty-like spectra but with 1,013/937 nm ratios <1.0	sol 3643, mcam03029	Only seen within the Amapari marker band and its float rocks	Hydration in dust at certain viewing geometries
K. Long, negative NIR slope*	Positive 527 nm band depths; continuously negative slopes from 676 nm or 751–1,013 nm; sometimes exhibits positive 867 nm band	sol 3606, mcam02817	Seen in Sutton Island, Glasgow, clay-sulfate transition, and Catrimani	Targets with strong diagenetic overprints; primarily ferrous component; hematite and/or goethite; secondary iron-rich mineral (nontronite and/or amorphous Fe-sulfate)
L. Convex profile with small 1,012/867 nm ratios*	Convex profile; 1,012/867 nm ratios <1.0; 527 nm band depths close to 0; negative 867 nm band depths.	sol 3642, mcam03022	Only seen within the Amapari marker band and its float rocks	Clinopyroxene
M. Flat profile with small 1,013/937 nm ratios*	Flat profile; 1,013/937 nm ratios <1.0; no obvious peaks; red/blue ratios close to 1.0	sol 3423, mcam01696	Primarily of dark surfaces on the Greenheugh Pediment	Relatively unaltered basaltic mineralogy with magnetite and possibly microplaty hematite

937 nm < 1.0 may be attributable with the broad, weak band around 1,000 nm inherent to magnetite, olivine, and/or pyroxene (Figure 5).

5.3.4. Consulting Laboratory Mixtures to Assess Mg-Sulfate Influence

The results of our experimental mixtures, along with localities and chemical data, support that a small (<1.0) 1,013/937 nm ratio in spectra from the clay-sulfate transition is not consistent with Mg-sulfates. However, this does not mean that there are no Mg-sulfates present, considering the ease at which the narrow hydration feature near 1,000 nm is masked in Mastcam wavelengths; spectra without R6 downturns, therefore, should not be considered “Mg-sulfate-free.” The ~1,000 nm feature is present in the laboratory spectra of 95/05 and 90/10

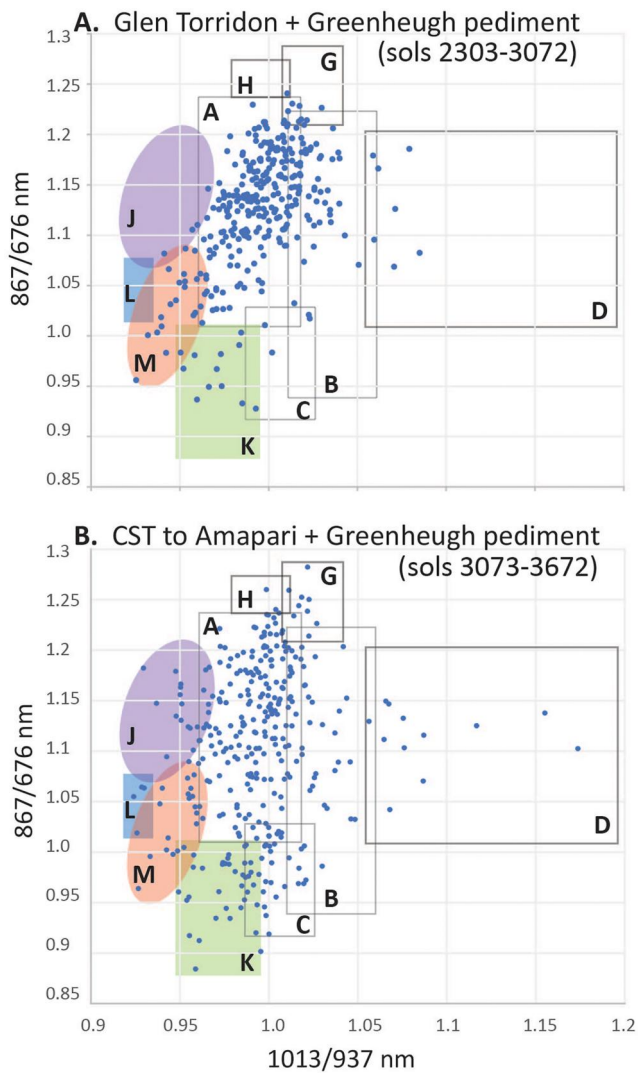


Figure 14. 1,013/937 nm ratio plotted against the 867/676 nm ratio with class regions for observations in (a) Glen Torridon and Greenheugh pediment; and (b) the clay-sulfate transition through the first encounter with Amapari and Greenheugh pediment. Regions outlined in light gray are pre-established classes using Mastcam spectra from landing to Vera Rubin ridge (Rice et al., 2022). Colored regions are newly defined classes using data collected post VRr: purple is Class J, green is Class K, blue is Class L, and red is Class M. Regions correspond to classes in Figure 13. 1,013/937 nm ratios less than 1 with otherwise flat NIR profiles are consistent with a hydration band at ~980 nm (Rice et al., 2010). The 867/676 nm ratio characterizes spectral shape and helps distinguish flatter spectra from peaks or shoulders. Note that the pre-established classes “Dark Fe- and/or Mn- oxides,” “Gray, flat NIR profile,” and “Iron meteorites” are not highlighted by these spectral parameters.

epsomite-saponite, the 95/05 epsomite-saponite with 5 wt.% basalt, and the epsomite-montmorillonite mixtures. However, Mastcam would not detect some of these features (i.e., spectra convolved to Mastcam bandpasses do not have an R6 downturn) due to (a) the positive NIR slopes of montmorillonite and saponite increasing the reflectance of the right shoulder of the 1,000 nm feature in epsomite and (b) the saponite and basalt reducing the band depth of the 1,000 nm feature in epsomite. It is challenging to attribute the feature in the epsomite-montmorillonite mixtures to just epsomite, considering that montmorillonite also has a small hydration feature around 1,000 nm as well (Figure 6). In the ASD spectra of 95/05 and 90/10 epsomite-nontronite mixtures, the 1,000 nm feature inherent to epsomite slightly overprints on the broader 900 nm band inherent to nontronite and is not likely to be detectable by Mastcam. CheMin identified the crystalline Mg-sulfate, starkeyite ($\text{MgSO}_4 \cdot 4\text{H}_2\text{O}$), in the Canaima drill (see Section 5.4 below). However, hydrated Mg-sulfates with less structurally bound water molecules than epsomite are expected to require even less of these other materials to mask their 1,000 nm hydration features. Thus, it is unlikely that Mastcam will be able to detect a hydrated Mg-sulfate unless the target is near pure hydrated Mg-sulfate (e.g., crystal, vein).

5.4. Classification of CheMin Target Drill Fines

During the traverse from Glen Torridon to the first encounter with the Amapari marker band, *Curiosity* drilled 17 outcrop targets that were analyzed by the CheMin instrument (Table 5, Figure 19). Specific mineralogical abundances are in Table S4. We use Mastcam spectra of the drill tailings to assign a spectral class and further characterize the mineralogy that is contributing to the spectral shapes. We acknowledge that spectra from drill tailings are flatter than others (lower 751/445 nm ratio) and have generally deeper absorption features than dusty counterparts, with the exception of hematite-rich targets (Rice et al., 2022). Consistent with their masking effects, high contributions of phyllosilicates (26–34 wt.%) characterize spectra of drill fines classified as A (Figure 19), which are localized to the Glen Torridon member, Knockfarrill hill. Aberlady and Kilmarie, drills from the Jura member of Glen Torridon, are classified as Class B, likely because Jura was found to have less phyllosilicates and more iron oxides compared to Knockfarrill hill (Thorpe et al., 2022). Spectra of the Edinburgh (EB) drill fines are classified as Class E which is consistent with the 14 wt.% magnetite identified by CheMin (Figure 19). Both magnetite (12.4 wt.%) and hematite (4.8 wt.%) characterize the spectra of the Hutton (HU) drill fines, which are classified as M (Figure 19). The flatness of the Hutton spectra in comparison to the **Edinburgh spectra may be attributable to more MnO in Edinburgh (Thompson, Spray, Gellert, et al., 2022; Thompson, Spray, O’Connell-Cooper, et al., 2022) and coarse-grained microplaty hematite in Hutton. Spectra of coarse grain sizes of hematite, which are gray in color, display small to negative 867 nm band depths and 640/527 nm ratios closer to 1.0 in comparison to red crystalline hematite (Horgan et al., 2020; Lane et al., 2002). Avanavero (AV) and MG have similar mineralogical proportions but are classified as B and C, respectively (Figure 19). The different classifications of Avanavero and MG may be attributable to the slightly higher amount of goethite in Avanavero and/or different amorphous materials (e.g., proportions of Mg- and or Fe- sulfates (Clark et al., 2023)). All CheMin targets classified as C have some goethite and hematite, which is consistent with the minerals’ convolved VNIR reflectance peaks at 751 nm. No drill fines included in this study and analyzed by CheMin are classified as the new classes J, K, or L.

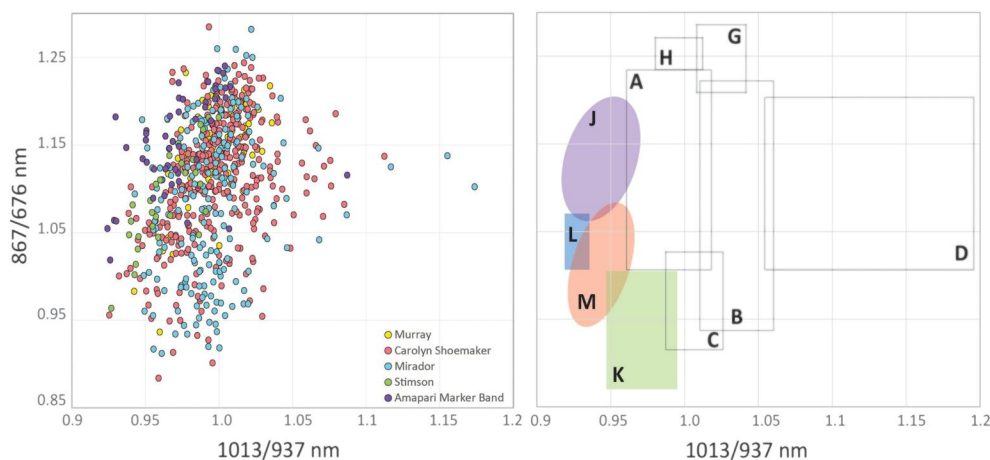


Figure 15. (left) Parameter plot in Figure 14 with point color-coded by formation or feature. (right) Class regions. Mirador displays the most variability and has the greatest amount of rock spectra plotting in Classes K and C; rock spectra from Stimson are consistent with Class M; rock spectra from Amapari marker band are consistent with Classes J and L.

5.5. Classification of APXS DRT Targets

We find that multiple classes exhibit trends with APXS elemental data. Elemental data of each DRT target included in this study is detailed in Table S5. Classes J, E, and M are often distinct from other classes in their elemental abundances (Figure 20; Table 6). Classes J and E are consistent with elemental trends of the Amapari marker band. The elevated and variable metals (Zn, FeO, MnO) and lack of an MgSO_4 trend in the rhythmic marker band characterizes Classes J and majority of E (Thompson et al., 2023). The target classified as E that has even higher amounts of MnO, FeO, and Zn (Sol 3642 Mel) is the only APXS target on the rippled unit of the Amapari marker band in this data set (Figure 20). Class M is consistent with elemental abundances of the Greenheugh pediment (e.g., elevated alkalis, MnO, and MgO; Thompson, Spray, Gellert, et al., 2022; Thompson, Spray, O'Connell-Cooper, et al., 2022). Class F displays similar elemental abundances to Class M but with lower total alkalis, but because only one APXS target was classified as such, we cannot draw a definitive conclusion on its elemental abundances. The slight increase in K_2O seen in spectra classified as K may be consistent with the presence of jarosite, which agrees with our interpretation of a possible Fe-sulfate contribution (see Section 5.3), though could also simply be reconciled by basaltic mineralogy. Notably, the trendline for the spectra classified as C in the SO_3 versus MgO plot is close to that of MgSO_4 (Figure 20), which is consistent with targets in the Mirador formation in the clay-sulfate transition. Spectra classified as C exhibit small 867–900 nm band depths with weak/flat right shoulders that appear as 1,012/867 nm ratios close to 1.0 which may be attributable to the flat spectrum of Mg-sulfates reducing the positive slope from 867 to 1,012 nm characteristic of the Fe^{3+} absorption around 867–900 nm.

5.6. ChemCam Passive Spectra

During *Curiosity's* traverse from Glen Torridon to first encounter with the Amapari marker band, ChemCam passive and Mastcam multispectral observations have not frequently been acquired on the same rock target. Thus, we are unable to perform comprehensive, direct comparisons of these data sets (such as the covariance analysis of Seeger (2020) from earlier in the traverse). However, we have selected a subset of measurements on like-surfaces (Figure 21) to further support the presence of new multispectral rock classes by comparing the parameters in Table S6 in Supporting Information S1. Upon visual inspection, the Mastcam and ChemCam passive spectra of representative targets (Table S7 in Supporting Information S1) of new Mastcam spectral rock classes agree (Figure 21). For targets representative of new Mastcam multispectral rock Classes J, K, and L, the slopes from 751 to 805 nm are closely matched (Figure 21; Table S8 in Supporting Information S1). The 751–805 nm slope for targets representative of Class M differ slightly (Figure 21; Table S8 in Supporting Information S1), potentially due to a broader left shoulder corresponding to the 867 nm band depth in the ChemCam passive spectrum or viewing geometry. However, both the ChemCam passive and Mastcam multispectral observation representative of Class M do exhibit reductions in slope around 640 nm. Measurements across both instruments all show positive

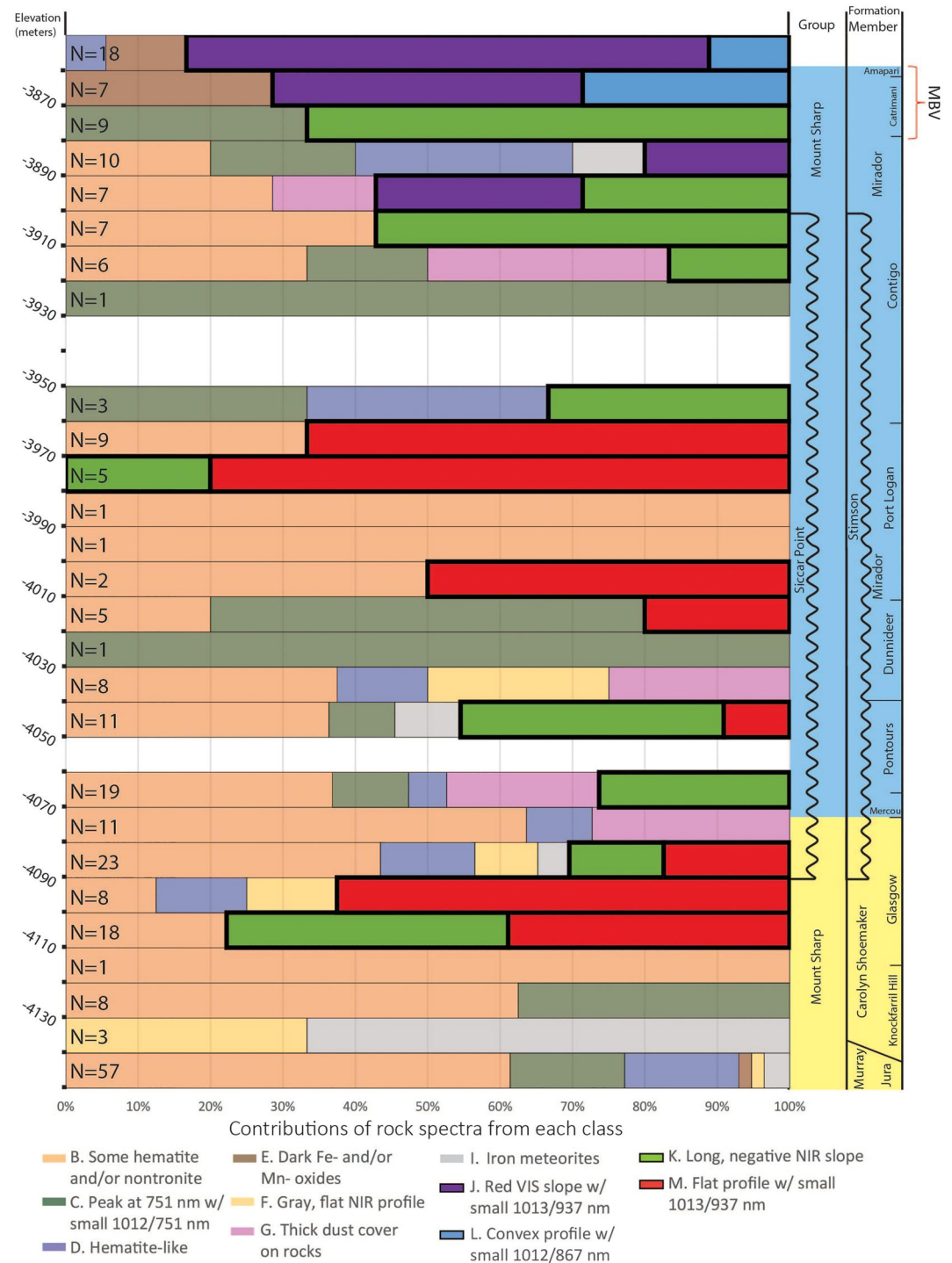


Figure 16. Distribution of rock spectral classes with elevation across *Curiosity*'s traverse from Glen Torridon to first encounter with the Amapari marker band (omitting the Neutral/Dusty class) with newly identified classes in bold. MBV = Marker Band Valley. Data are binned to 10 m elevation intervals. Percentage values indicate proportions of rock spectra belonging to each class within the elevation bin. Classes J and L are localized to Amapari marker band. Class M is consistent with excursions onto Greenheugh pediment and float rocks in its approach. Class K corresponds to regions with diagenetic overprints and features (Figure 19).

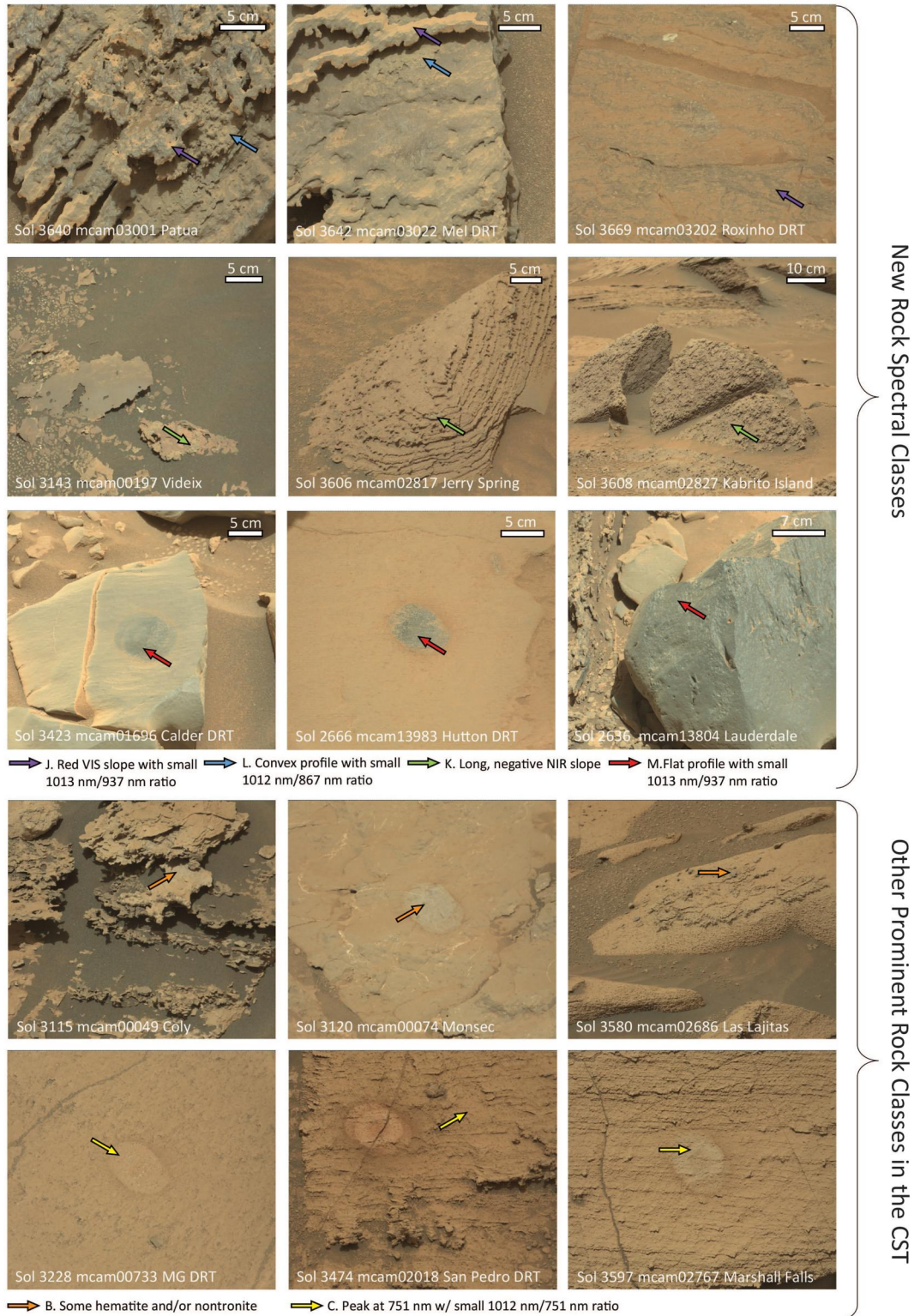


Figure 17.

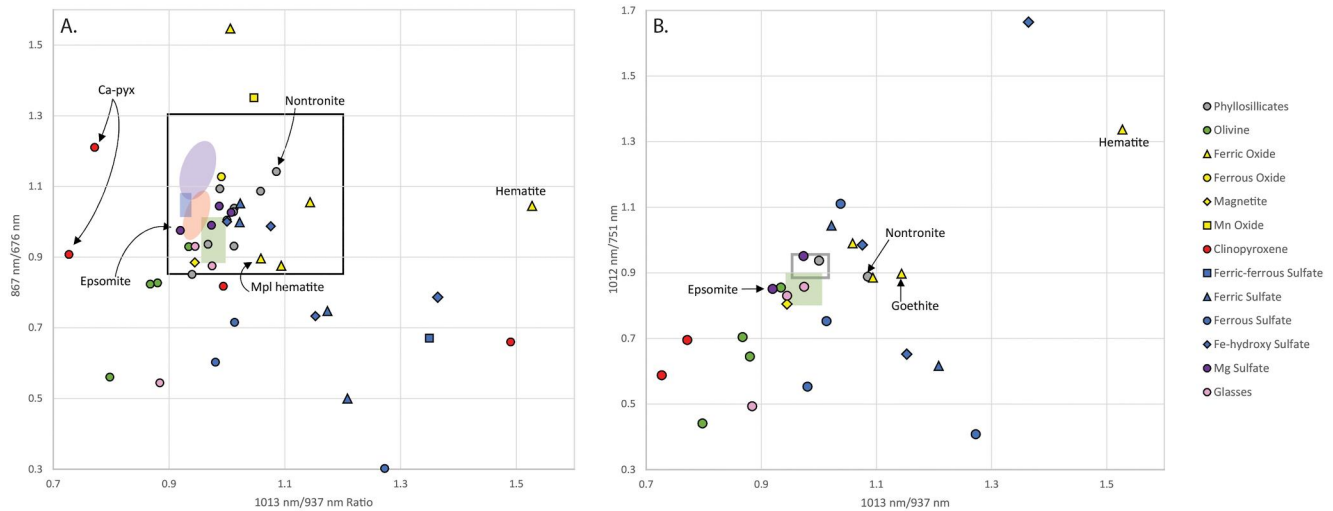


Figure 18. Parameter plot of pure mineral spectra using (a) 1,013/937 and 867/676 nm ratios and (b) 1,013/937 and 1,012/751 nm ratios. A select few minerals are shown in (b) in order to further contextualize Class K. The box outlined in black in (a) is the parameter space that Mastcam observations from sols 2303–3672 encompass. Colored regions correspond with new classes like in Figure 14; purple is Class J, blue is Class L, red is Class M, green is Class K. Mpl = microplaty. Gray outline in (b) encompasses class C and is highlighted in order to distinguish mineralogic interpretations between classes K and C. We included minerals that characterize the Mastcam and Mastcam-Z rock spectral classes defined by Rice et al. (2022, 2023), and generally expected minerals that may show signatures in Mastcam spectra: phyllosilicates, olivine, iron oxides, clinopyroxenes, sulfates, and glasses from the Mastcam-Z reference library (Rice et al., 2023; Table S3).

527 or 535 nm band depths (Figure 21; Table S8 in Supporting Information S1), though Classes J and L have more significant differences, possibly due to differences in the amounts of dust between ROI. Overall, the agreement between the two spectral data sets give confidence that the Mastcam spectral characteristics described here are attributable to real compositional properties of the rocks (and are not significantly influenced by calibration uncertainties, viewing geometry effects, or instrumental artifacts).

5.7. Implications for Alteration Processes in the Clay-Sulfate Transition

After exploring mudstones and clay-bearing strata that reflect wetter depositional environments, *Curiosity's* traverse in the clay-sulfate transition marks a transition to a drier environment with intermittently wetter periods (Rapin et al., 2023). Diagenetic features in the clay-sulfate transition exhibit significant Mg-sulfate enrichments that are likely amorphous with probable contributions of Fe-sulfates (Smith et al., 2022). We propose that these components, along with basaltic materials and small amounts of iron-oxides, can be characterized by our spectral Class K, thus enhancing our understanding of alteration processes in the clay-sulfate transition. The following could explain our hypothesized assemblage that characterizes Class K. The oxidation of Fe-sulfides under a CO₂ atmosphere advances the alteration of silicates (e.g., dissolution of olivine) which release Ca²⁺, Mg²⁺, and Fe²⁺ cations that can be included in Ca-, Mg-, and Fe- sulfates (Dehouck et al., 2014; Yu et al., 2022). Additionally, the oxidation of Fe-sulfides results in fluids with low pH, which either prevented the formation of phyllosilicates or dissolved them in the clay-sulfate transition (Bigham & Nordstrom, 2000; Bibring et al., 2006; Zolotov & Mironenko, 2007). Crystalline Fe-sulfate has not been detected by CheMin in the clay-sulfate transition but SAM-EGA identifies a broad SO₂ release, implying that Fe-sulfate must be present in the amorphous phase (Clark et al., 2023). Amorphous ferrous sulfates are expected to oxidize and/or crystallize rapidly under Martian conditions (Sklute et al., 2015). However, iron sulfides that had oxidized to ferrous sulfates could form Fe-hydroxy sulfates if the ferrous sulfates dehydrated rapidly before ferrous ions could undergo any oxidation that would

Figure 17. The first three rows show examples of primary surface types in each newly defined class. Class J, “Red VIS slope with small 1,013 nm/937 nm ratio,” is inherent to the rippled and rhythmically laminated units of the Amapari marker band. Class L, “Convex profile with small 1,012 nm/867 nm ratio,” is inherent to relatively lighter toned surfaces on the rippled unit of the Amapari marker band. Class K, “Long, negative NIR slope,” is inherent to surfaces with strong diagenetic overprints. Class M, “Flat profile with small 1,013 nm/937 nm ratio,” class is inherent to dark gray surfaces on the Greenheugh pediment and floats in its approaches. The last two rows show examples surface types inherent to two other prominent classes in the clay-sulfate transition. Regions of interest (ROIs) comprise a unique color which can result in small and specific ROIs, however we try to create ROIs with a minimum size of 30 pixels following Rice et al. (2022).

Table 5

Summary of Chemistry and Mineralogy (CheMin) Samples (Cardenas et al., 2023; Rampe et al., 2023; Thorpe et al., 2022) and the Mastcam Spectral Classes Assigned to Their Associated Drill Tailings And/Or Dump Piles

Abbreviation	CheMin sample	Sol(s)	Formation	Proposed depositional environment	Mastcam rock spectral class
AL	Aberlady	2,370	Murray	Lacustrine	B. Some hematite and/or nontronite
KM	Kilmarie	2,384	Murray	Lacustrine	B. Some hematite and/or nontronite
GE1	Glen Etive	2,486	Carolyn Shoemaker	Fluvial	A. Neutral/Dusty
GE2	Glen Etive 2	2,527	Carolyn Shoemaker	Fluvial	A. Neutral/Dusty
HU	Hutton	2,669	Carolyn Shoemaker	Lacustrine/lake margin	M. Flat profile w/small 1,013/937 nm ratio
EB	Edinburgh	2,713	Stimson	Ancient aeolian	E. Dark Fe- and/or Mn- oxides
GG	Glasgow	2,754	Carolyn Shoemaker	Lacustrine/lake margin	C. Peak at 751 nm w/small 1,012/751 nm ratio
MA	Mary Anning	2,838	Carolyn Shoemaker	Fluvial	A. Neutral/Dusty
MA3	Mary Anning 3	2,870	Carolyn Shoemaker	Fluvial	A. Neutral/Dusty
GR	Groken	2,912	Carolyn Shoemaker	Fluvial	A. Neutral/Dusty
NT	Nontron	3,055	Carolyn Shoemaker	Fluvio-lacustrine	B. Some hematite and/or nontronite
BD	Bardou	3,094	Carolyn Shoemaker	Fluvio-lacustrine	D. Hematite-like
PT	Pontours	3,170	Carolyn Shoemaker	Fluvio-lacustrine	B. Some hematite and/or nontronite
MG	Maria Gordon	3,226	Mirador	Eolian	C. Peak at 751 nm w/small 1,012/751 nm ratio
ZE	Zechstein	3,289	Mirador	Eolian	B. Some hematite and/or nontronite
AV	Avanavero	3,509	Mirador	Eolian	B. Some hematite and/or nontronite
CA	Canaima	3,612	Mirador	Eolian	C. Peak at 751 nm w/small 1,012/751 nm ratio

change its valency state (Bigam & Nordstrom, 2000; Paramanick et al., 2021). Alternatively, amorphous ferric sulfates have been found to form from rapid dehydration of saturated solutions (Xu & Parise, 2012). Intermittent flowing water could have dissolved the Mg-sulfates, given their high solubility in water, and then once the sulfate-rich water table approached the surface, Mg-sulfates could have formed into nodules and cements and then become amorphous due to rapid dehydration, like the amorphous Fe-sulfates (Rapin et al., 2023; Vaniman et al., 2004). Thus, to characterize Class K, we hypothesize that a mixture of Mg- and Fe- sulfates cemented basaltic grains together as a wetter environment dried; and that the goethite and hematite components could have formed from the further aqueous alteration of Fe-sulfates (Davidson et al., 2008; Schwertmann & Murad, 1983).

5.8. Implications for Mg-Sulfate Detections

We recognize that CheMin has not detected Mg-sulfate and phyllosilicate in the same sample. However, orbital data suggests that both Mg-sulfate (likely in the amorphous phase) and phyllosilicates are present in Glen Torridon and up section where *Curiosity* is planned to explore (Sheppard, Milliken, et al., 2021; Sheppard, Thorpe, et al., 2021). The abundance of phyllosilicates in Glen Torridon easily masks the presence of Mg-sulfates (this study; Sheppard et al., 2022). Although, Glen Torridon is likely the most clay-rich unit *Curiosity* will encounter considering the rover has since traversed further up Mount Sharp into aeolian deposits and drier depositional settings. Thus, the results of our laboratory mixture experiment can be applied to *Curiosity's* future traverse but will likely be most applicable in assessing the purity of a potential Mg-sulfate-rich, light-toned, diagenetic feature (e.g., veins, crystals).

5.9. General Trend Across Instruments

While new classes J, L, and M, characterize the marker band and the Greenheugh Pediment, most of the clay-sulfate transition can be characterized by pre-existing classes. This is in agreement with the APXS finding that concentration of elements in the bedrock of the clay-sulfate transition is very similar to underlying Mt. Sharp units (Berger et al., 2023). APXS did not find evidence of an increase in Mg-sulfate in the bedrock that couldn't be attributed to nodules (Berger et al., 2023), which supports our interpretations of Classes K and C. Furthermore, ChemCam shows that bulk bedrock in the clay-sulfate transition is increased in sulfate content compared to underlying bedrock but that the nodular textures drive this trend (Rapin et al., 2023).

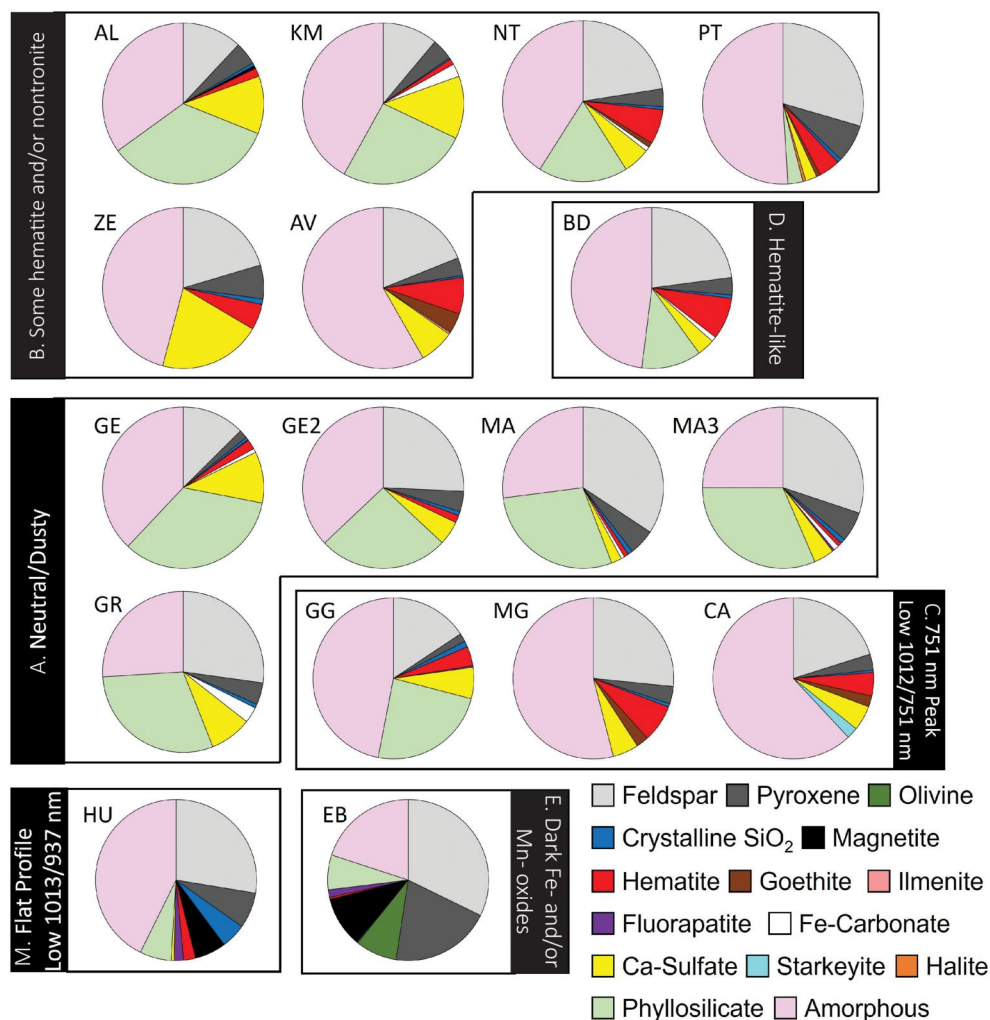


Figure 19. Mineral abundances of Chemistry and Mineralogy samples (Rampe et al., 2023; Thorpe et al., 2022) grouped by Mastcam spectral class. Sample locations and name abbreviations are defined in Figure 2. Mastcam spectral classes are based on spectral features of the drill tailings and/or dump piles from each sample.

6. Conclusions

It was previously hypothesized that Mastcam would be able to detect hydrated minerals, and even distinguish between mono-hydrated versus poly-hydrated Mg-sulfate phases (e.g., kieserite vs. epsomite), as *Curiosity* approached the sulfate-bearing strata of Mt. Sharp (Rice et al., 2022). This study provides new insight that Mastcam is sensitive to a weak hydration feature in Mg-sulfates near 1,000 nm which produces a “downturn” in the R6 filter (a 1,012/937 nm slope <1.0). Our laboratory investigation, however, shows that detecting Mg-sulfate in Mastcam multispectral data would be challenging. Specifically, 90–95 wt.% epsomite would be required to be detectable in Mastcam spectra of two-phase mixtures with phyllosilicates. Additionally, just 5 wt.% additions of basalt dampen any notable spectral features in these mixtures. Thus, any R6 downturns present in Mastcam multispectral data from the sulfate-bearing unit that *Curiosity* continues to explore can more easily be attributed to other minerals. In fact, we find that the Mastcam spectra from confirmed Mg-sulfate-bearing strata consistently do not exhibit a R6 downturn or other spectral features uniquely attributable to sulfates. The results of our laboratory investigation confirm our hypothesis that it would take small amounts of phyllosilicates and/or basalt to completely mask the R6 downturn in Mastcam spectra.

We continued the compilation of a comprehensive database for Mastcam spectra since the work of Rice et al. (2022) and their analysis through VRr (sols 0–2302). We analyzed observations from Glen Torridon,

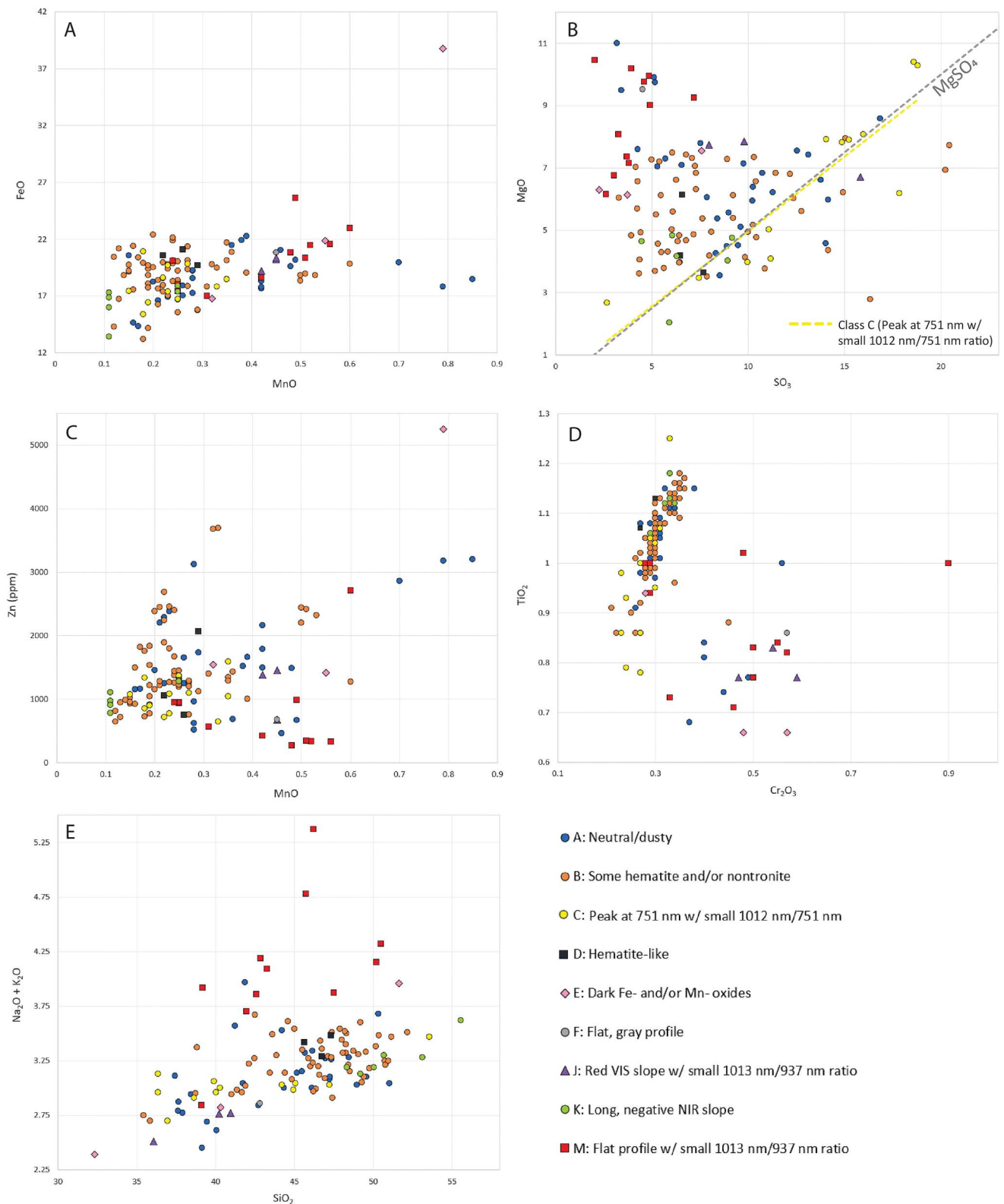


Figure 20. Comparisons of Mastcam spectral classes from Dust Removal Tool (DRT) targets to Alpha Particle X-ray Spectrometer (APXS) elemental compositions from Thompson et al. (2023) and Berger et al. (2023). Each APXS measurement on a DRT was color-coded by its corresponding Mastcam rock spectral class, if there was a corresponding multispectral observation acquired and the spectra of the DRT could be classified.

Table 6
Alpha Particle X-Ray Spectrometer (APXS) Elemental Data Averaged for Each Class

	A. Neutral/dusty	B. Some hematite and/or nontronite	C. Peak at 751 nm with small 1,012/751 nm	D. Hematite-like	E. Dark Fe- and/or Mn- oxides	F. Flat, gray profile	J. Red VIS slope with small 1,013/937 nm	K. Long, negative NIR slope	M. Flat profile with small 1,013/937 nm
N	28	56	12	3	3	1	3	6	11
Na ₂ O	2.38 ± 0.15	2.40 ± 0.14	2.24 ± 0.16	2.54 ± 0.16	2.44 ± 0.16	2.45 ± 0.14	2.22 ± 0.20	2.38 ± 0.14	3.00 ± 0.14
MgO	6.76 ± 0.20	5.55 ± 0.17	6.48 ± 0.20	4.65 ± 0.17	6.66 ± 0.20	9.53 ± 0.25	7.44 ± 0.22	4.08 ± 0.14	8.56 ± 0.21
Al ₂ O ₃	8.22 ± 0.21	8.51 ± 0.20	7.74 ± 0.24	8.55 ± 0.19	7.53 ± 0.22	8.23 ± 0.19	6.60 ± 0.22	9.22 ± 0.22	8.62 ± 0.22
SiO ₂	43.91 ± 0.54	46.17 ± 0.54	41.96 ± 0.53	46.57 ± 0.54	41.42 ± 0.50	42.80 ± 0.54	39.08 ± 0.50	51.15 ± 0.56	44.46 ± 0.50
P ₂ O ₅	0.97 ± 0.07	1.01 ± 0.07	1.12 ± 0.08	1.10 ± 0.07	0.83 ± 0.06	0.73 ± 0.05	0.70 ± 0.07	1.11 ± 0.07	0.80 ± 0.06
SO ₃	9.03 ± 0.18	8.25 ± 0.13	13.14 ± 0.24	6.91 ± 0.14	4.52 ± 0.12	4.53 ± 0.08	11.20 ± 0.21	6.81 ± 0.12	3.99 ± 0.08
Cl	1.44 ± 0.04	1.27 ± 0.03	1.01 ± 0.038	1.20 ± 0.04	2.15 ± 0.05	1.77 ± 0.03	2.33 ± 0.05	1.02 ± 0.03	1.23 ± 0.03
K ₂ O	0.73 ± 0.03	0.85 ± 0.03	0.78 ± 0.03	0.86 ± 0.03	0.61 ± 0.03	0.41 ± 0.02	0.46 ± 0.03	0.90 ± 0.04	1.10 ± 0.04
CaO	6.02 ± 0.09	5.08 ± 0.07	5.59 ± 0.09	5.18 ± 0.07	5.74 ± 0.08	6.65 ± 0.07	7.83 ± 0.09	4.98 ± 0.06	5.88 ± 0.07
TiO ₂	1.00 ± 0.04	1.05 ± 0.04	0.96 ± 0.04	1.09 ± 0.04	0.75 ± 0.04	0.86 ± 0.03	0.79 ± 0.04	1.10 ± 0.05	0.88 ± 0.03
Cr ₂ O ₃	0.34 ± 0.02	0.31 ± 0.02	0.27 ± 0.03	0.29 ± 0.02	0.44 ± 0.03	0.57 ± 0.03	0.53 ± 0.04	0.32 ± 0.02	0.47 ± 0.02
MnO	0.35 ± 0.02	0.25 ± 0.01	0.24 ± 0.02	0.26 ± 0.02	0.55 ± 0.03	0.45 ± 0.01	0.44 ± 0.03	0.16 ± 0.01	0.42 ± 0.02
FeO	18.43 ± 0.23	18.91 ± 0.23	18.09 ± 0.23	20.45 ± 0.26	25.79 ± 0.31	20.81 ± 0.26	19.91 ± 0.24	16.47 ± 0.20	20.36 ± 0.24
Ni	757.18 ± 43.21	861.45 ± 46.16	858.00 ± 48.33	830.00 ± 51.67	405.33 ± 40.00	357.00 ± 20.00	330.33 ± 35.00	936.83 ± 50.00	448.36 ± 27.27
Zn	1,618.79 ± 53.39	1,525.46 ± 49.38	1,039.08 ± 38.33	1,290.67 ± 46.67	2,738.67 ± 86.67	678.00 ± 25.00	1,174.00 ± 43.33	1,057.00 ± 33.33	799.64 ± 27.27
Br	613.39 ± 23.39	454.23 ± 17.23	376.25 ± 17.08	571.67 ± 21.67	1,196.00 ± 38.33	369.00 ± 15.00	1,442.00 ± 50.00	336.33 ± 12.50	186.45 ± 9.55

Note. N represents the number of spectra from APXS targets in each Mastcam rock spectral class.

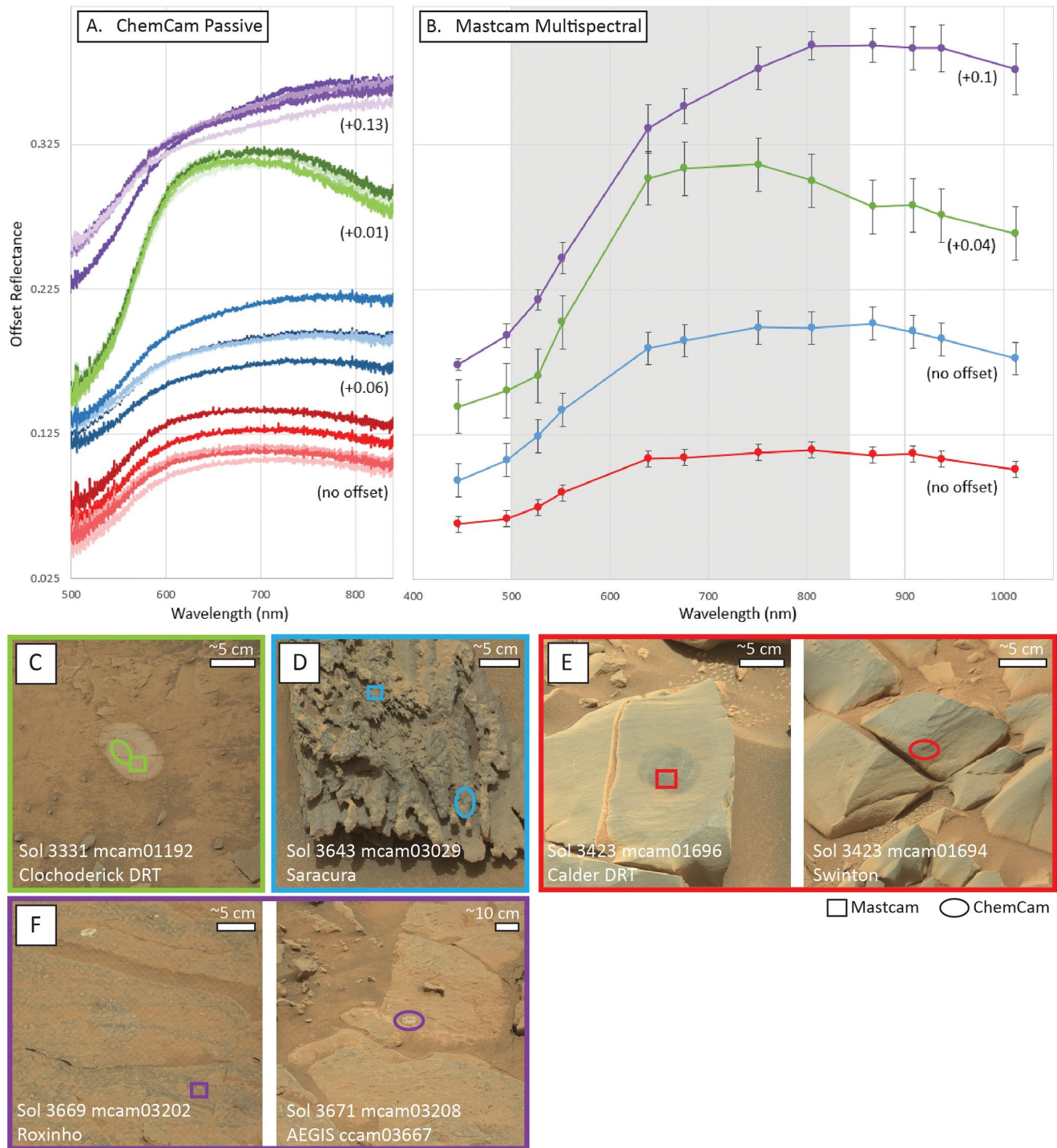


Figure 21. Comparison of (a) Chemistry and Camera (ChemCam) passive and (b) Mastcam multispectral observations on like-surfaces. The shaded region in the Mastcam spectral plot highlights the wavelength range of the ChemCam passive spectra shown (500–850 nm). The surfaces in which ChemCam passive and Mastcam spectra were acquired are shown by colored circles and boxes, respectively. The color of the shapes corresponds with the color of the spectra. Locations of Mastcam and ChemCam spectra for (c) Class K examples; (d) Class L examples; (e) Class M examples; and (f) Class J examples.

Greenheugh Pediment, and the clay-sulfate transition up to *Curiosity*'s first encounter of the Amapari marker band (sols 2303–3672). Through an investigation of spectral trends and variability with stratigraphy, we find that the clay-sulfate transition region exhibits more multispectral rock variability than the phyllosilicate-rich region, Glen Torridon, due to a higher abundance of iron-oxides and lower abundance of phyllosilicates. We also identify four

new rock spectral classes that are unique to this part of the traverse. Two of these new classes, Classes J and L, are associated with the Amapari marker band, and their spectral characteristics are attributable to Ca-pyroxenes in the bedrock and to dust coatings on the rippled and rhythmically laminated units. Another new spectral class, Class M, is associated with the Greenheugh Pediment and is consistent with relatively unaltered basalt with magnetite. The new rock class, Class K, inherent to the clay-sulfate transition and MBV indicates a strong diagenetic overprint spanning these regions. The occurrence of this class is consistent with the hypothesis of alternating wet-dry environments in the clay-sulfate transition producing sulfate-rich nodules (Rapin et al., 2023), which are driving some of the Mastcam multispectral variability. These new spectral classes, in addition to those identified in previous traverse regions (Rice et al., 2022), will provide a baseline for *Curiosity's* ongoing investigation of Mount Sharp and also for Perseverance's exploration of Jezero crater, another Noachian-aged lake system.

Data Availability Statement

All of the Mastcam multispectral image data used in this manuscript are freely available through the Planetary Data System Cartography and Imaging Sciences node (<https://pds-imaging.jpl.nasa.gov/volumes/msl.html>). Our Mastcam multispectral database including spectra with geologic metadata, composite images, ROIs, and ROI context images are available in Rice (2022) and Eng et al. (2023).

References

- Banham, S. G., Gupta, S., Rubin, D. M., Bedford, C. C., Edgar, L. A., Bryk, A. B., et al. (2022). Evidence for fluctuating wind in shaping an ancient Martian Dune field: The Stimson formation at the Greenheugh pediment, Gale Crater. *Journal of Geophysical Research: Planets*, 127(9), e2021JE007023. <https://doi.org/10.1029/2021JE007023>
- Bell, J. F., III, Godber, A., McNair, S., Caplinger, M. A., Maki, J. N., Lemmon, M. T., et al. (2017). The Mars Science Laboratory *Curiosity* rover Mastcam instruments: Preflight and in-flight calibration, validation, and data archiving. *Earth and Space Science*, 4(7), 396–452. <https://doi.org/10.1002/2016EA000219>
- Bell, J. F., Malin, M. C., Caplinger, M. A., Ravine, M. A., Godber, A. S., Jungers, M. C., & Rice, M. S. (2012). Mastcam multispectral imaging on the Mars science laboratory rover: Wavelength coverage and imaging strategies at the Gale Crater field site. In *43rd lunar and planetary science conference*.
- Bellucci, G., Altieri, F., Bibring, J. P., & the OMEGA Team. (2004). The OMEGA instrument on board Mars express: First results. *Memorie della Società Astronomica Italiana Supplement*, 5, 27.
- Bennett, K. A., Fox, V. K., Bryk, A., Dietrich, W., Fedo, C., Edgar, L., et al. (2023). The *Curiosity* rover's exploration of glen torridon, Gale Crater, Mars: An overview of the campaign and scientific results. *Journal of Geophysical Research: Planets*, 128(1), e2022JE007185. <https://doi.org/10.1029/2022JE007185>
- Berger, J. A., Gellert, R., McCraig, M. A., O'Connell-Cooper, C. D., Spray, J. G., Thompson, L. M., et al. (2023). Isochemical characteristics of the CST in Gale crater, Mars: APXS results from Mont Mercou to the marker Band valley. In *54th lunar and planetary science conference 2806*.
- Bibring, J.-P., Langevin, Y., Mustard, J. F., Poulet, F., Arvidson, R., Gendrin, A., et al. (2006). Global mineralogical and aqueous Mars history derived from OMEGA/Mars express data. *Science*, 312(5772), 400–404. <https://doi.org/10.1126/science.1122659>
- Bigham, J. M., & Nordstrom, D. K. (2000). Iron and aluminum hydroxysulfates from acid sulfate waters. In *Reviews in mineralogy and geochemistry* (Vol. 40). <https://doi.org/10.2138/rmg.2000.40.7.351403>
- Bishop, J., Bell, J., & Moersch, J. (Eds.) (2019). *Remote compositional analysis: Techniques for understanding spectroscopy, mineralogy, and geochemistry of planetary surfaces* (Cambridge planetary science). Cambridge University Press. <https://doi.org/10.1017/9781316888872>
- Bishop, J. L., Yeşilbaş, M., Talla, D., & Hiroi, T. (2021). Spectral properties of Fe hydroxy sulfates and implications for Mars. In *52nd lunar and planetary science conference 2548*.
- Blake, D., Vaniman, D., Achilles, C., Anderson, R., Bish, D., Bristow, T., et al. (2012). Characterization and calibration of the CheMin mineralogical instrument on Mars science laboratory. *Space Science Reviews*, 170(1–4), 341–399. <https://doi.org/10.1007/s11214-012-9905-1>
- Bridges, J. C., Schwenger, S. P., Leveille, R., Westall, F., Wiens, R. C., Mangold, N., et al. (2015). Diagenesis and clay mineral formation at Gale Crater, Mars. *Journal of Geophysical Research: Planets*, 120(1), 1–19. <https://doi.org/10.1002/2014JE004757>
- Bristow, T. F., Kennedy, M. J., Derkowski, A., Droser, M. L., Jiang, G., & Creaser, R. A. (2009). Mineralogical constraints on the paleoenvironments of the Ediacaran Doushantuo formation. *Proceedings of the National Academy of Sciences of the United States of America*, 106(32), 13190–13195. <https://doi.org/10.1073/pnas.0901080106>
- Bristow, T. F., Rampe, E. B., Achilles, C. N., Blake, D. F., Chipera, S. J., Craig, P., et al. (2018). Clay mineral diversity and abundance in sedimentary rocks of Gale crater, Mars. *Science Advances*, 4(6), eaar3330. <https://doi.org/10.1126/sciadv.aar3330>
- Bristow, T. F., & Milliken, R. (2011). A terrestrial perspective on authigenic clay production in ancient Martian lakes. *Clays and Clay Minerals*, 59(4), 339–358. <https://doi.org/10.1346/CCMN.2011.0590401>
- Broz, A. P. (2020). Organic matter preservation in ancient soils of Earth and Mars. *Life*, 10(7), 113. <https://doi.org/10.3390/life10070113>
- Burns, R. (1993). Mineralogical applications of crystal field theory. In *Cambridge topics in mineral physics and chemistry* (2nd ed.). Cambridge University Press. <https://doi.org/10.1017/CBO9780511524899>
- Buz, J., Ehlmann, B. L., Pan, L., & Grotzinger, J. P. (2017). Mineralogy and stratigraphy of the Gale crater rim, wall, and floor units. *Journal of Geophysical Research: Planets*, 122(5), 1090–1118. <https://doi.org/10.1002/2016JE005163>
- Campbell, J. L., King, P. L., Burkemper, L., Berger, J. A., Gellert, R., Boyd, N. I., et al. (2014). The Mars Science Laboratory APXS calibration target: Comparison of Martian measurements with the terrestrial calibration. *Nuclear Instruments and Methods in Physics Research Section B: Beam Interactions with Materials and Atoms*, 323, 49–58. <https://doi.org/10.1016/j.nimb.2014.01.011>
- Campbell, J. L., Perrett, G. M., Gellert, R., Andrushenko, S. M., Boyd, N. I., Maxwell, J. A., et al. (2012). Calibration of the Mars Science Laboratory alpha particle X-ray spectrometer. *Space Science Reviews*, 170(1–4), 319–340. <https://doi.org/10.1007/s11214-012-9873-5>

Acknowledgments

This research was carried out at Western Washington University and under a contract with the National Aeronautics and Space Administration (80NM0018D0004). The data presented here were collected thanks to the MSL Science Team, the specialists at Malin Space Science Systems, and the calibration crew at Arizona State University. We also thank those who have contributed to the Mastcam multispectral database while students at Western Washington University. Liz Rampe, Lucy Thompson, and Jeff Johnson provided assistance with CheMin, APXS, and ChemCam data, respectively. Thank you to Valerie Fox and an anonymous reviewer for your comments that improved the manuscript.

- Cardenas, B. T., Grotzinger, J. P., Lamb, M. P., Lewis, K. W., Fedo, C. M., Bryk, A. B., et al. (2023). Barform deposits of the Carolyn Shoemaker formation, Gale crater, Mars. *Journal of Sedimentary Research*, 92(12), 1071–1092. <https://doi.org/10.2110/jsr.2022.032>
- Carter, J., Loizeau, D., Mangold, N., Poulet, F., & Bibring, J.-P. (2015). Widespread surface weathering on early Mars: A case for a warmer and wetter climate. *Icarus*, 248, 373–382. <https://doi.org/10.1016/j.icarus.2014.11.011>
- Chipera, S. J., & Bish, D. L. (2002). FULLPAT: A full-pattern quantitative analysis program for X-ray powder diffraction using measured and calculated patterns. *Journal of Applied Crystallography*, 35(6), 744–749. <https://doi.org/10.1107/s0021889802017405>
- Clark, J. V., Sutter, B., Lewis, J., McAdam, A. C., Archer, P. D., Franz, H., et al. (2023). Mineralogical and chemical changes in the CST region as detected by the sample analysis at Mars-evolved Gas analyzer (SAM-EGA) in Gale crater, Mars. In *54th lunar and planetary science conference 2806*.
- Cloutis, E. A., Bell, J. F., & Mueller, T. (2000). Pyroxene + palagonite mixture spectra: Effects of palagonite on deriving pyroxene compositional information. In *31st lunar and planetary science conference 1114*.
- Cloutis, E. A., Hawthorne, F., Mertzman, S., Krenn, K., Craig, M., Marcino, D., et al. (2006). Detection and discrimination of sulfate minerals using reflectance spectroscopy. *Icarus*, 184(1), 121–157. <https://doi.org/10.1016/j.icarus.2006.04.003>
- Cloutis, E. A., Craig, M. A., Mustard, J. F., Kruezelecky, R. V., Jamroz, W. R., Scott, A., et al. (2007). Stability of hydrated minerals on Mars. *Geophysical Research Letters*, 34(20), L19201. <https://doi.org/10.1029/2007GL031267>
- Currey, D. R. (1990). Quaternary palaeolakes in the evolution of semidesert basins, with special emphasis on Lake Bonneville and the Great Basin, U.S.A. *Paleogeography, Palaeoclimatology, Paleoecology*, 76(3–4), 189–214. [https://doi.org/10.1016/0031-0182\(90\)90113-1](https://doi.org/10.1016/0031-0182(90)90113-1)
- Curtis, S. (2022). *Spectral variability in naturally weathered rock surfaces and implications for Mars (unpublished master's dissertation)*. WWU Graduate School Collection 1118. Retrieved from <https://cedar.wvu.edu/wwuet/1118>
- Das, D., Turner, S. M. R., Gasda, P. J., Schwenzer, S. P., Palandri, J., Reed, M. H., et al. (2023). Simulating evaporative wet and dry cycles in Gale crater, Mars using modeling techniques. In *54th lunar and planetary science conference 2806*.
- Davidson, L. E., Shaw, S., & Benning, L. G. (2008). The kinetics and mechanisms of schwertmannite transformation to goethite and hematite under alkaline conditions. *American Mineralogist*, 93(8–9), 1326–1337. <https://doi.org/10.2138/am.2008.2761>
- Day, M., Anderson, W., Kocurek, G., & Mohrig, D. (2016). Carving intracrater layered deposits with wind on Mars. *Geophysical Research Letters*, 43(6), 2473–2479. <https://doi.org/10.1002/2016GL068011>
- Dehouck, E., Cousin, A., Mangold, N., Frydenvang, J., Gasnault, O., Forni, O., et al. (2022). Bedrock geochemistry and alteration history of the clay-bearing Glen Torridon region of Gale crater, Mars. *Journal of Geophysical Research: Planets*, 127(12), e2021JE007103. <https://doi.org/10.1029/2021JE007103>
- Dehouck, E., McLennan, S. M., Meslin, P.-Y., & Cousin, A. (2014). Constraints on abundance, composition, and nature of X-ray amorphous components of soils and rocks at Gale crater, Mars. *Journal of Geophysical Research: Planets*, 119(12), 2640–2657. <https://doi.org/10.1002/2014JE004716>
- Dixon, D. (2018). *Visible-to-near-infrared spectral variability of hydrated sulfates and candidate Mars landing sites: Implications for the Mastcam-Z investigation on NASA's Mars-2020 rover Mission (Unpublished master's dissertation)*. WWU Graduate School Collection 638. Retrieved from <https://cedar.wvu.edu/wwuet/638>
- Douglas, S. (2004). Microbial biosignatures in evaporite deposits: Evidence from Death Valley, California. *Planetary and Space Science*, 52(1–3), 223–227. <https://doi.org/10.1016/j.pss.2003.08.005>
- Edgar, L. A., Fedo, C. M., Gupta, S., Banham, S. G., Fraeman, A. A., Grotzinger, J. P., et al. (2020). A lacustrine paleoenvironment recorded at Vera Rubin ridge, Gale crater: Overview of the sedimentology and stratigraphy observed by the Mars Science Laboratory Curiosity rover. *Journal of Geophysical Research: Planets*, 125(3), e2019JE006307. <https://doi.org/10.1029/2019JE006307>
- Eng, A., Rice, M. S., St. Clair, M., Million, C. C., Brown, S., Seeger, C., et al. (2023). Mastcam multispectral database from the Curiosity rover's traverse in the Gale crater, Mars (sols 2302–3672) [Dataset]. Geology Faculty Publications, 106. <https://doi.org/10.25710/grvp-1082>
- Farrand, W. H., Bell, J. F., III, Johnson, J. R., Arvidson, R. E., Crumpler, L. S., Hurowitz, J. A., & Schröder, C. (2008). Rock spectral classes observed by the Spirit rover's Pancam on the Gusev crater plains and in the Columbia Hills. *Journal of Geophysical Research*, 113(E12), E12S38. <https://doi.org/10.1029/2008JE003237>
- Farrand, W. H., Bell, J. F., III, Johnson, J. R., Rice, M. S., Jolliff, B. L., & Arvidson, R. E. (2014). Observations of rock spectral classes by the Opportunity rover's Pancam on northern Cape York and on Matijevic Hill, Endeavour Crater, Mars. *Journal of Geophysical Research: Planets*, 119(11), 2349–2369. <https://doi.org/10.1002/2014JE004641>
- Fedo, C. M., Bryk, A. B., Edgar, L. A., Bennett, K. A., Fox, V. K., Dietrich, W. E., et al. (2022). Geology and stratigraphic correlation of the Murray and Carolyn Shoemaker formations across the Glen Torridon region, Gale crater, Mars. *Journal of Geophysical Research: Planets*, 127(9), e2022JE007408. <https://doi.org/10.1029/2022JE007408>
- Fraeman, A. A., Johnson, J. R., Arvidson, R. E., Rice, M. S., Wellington, D. F., Morris, R. V., et al. (2020). Synergistic ground and orbital observations of iron oxides on Mount Sharp and Vera Rubin ridge. *Journal of Geophysical Research: Planets*, 125(9), e2019JE006294. <https://doi.org/10.1029/2019JE006294>
- Gasda, P. J., Comellas, J., Essunfeld, A., Das, D., Bryk, A. B., Dehouck, E., et al. (2022). Overview of the morphology and chemistry of diagenetic features in the clay-rich Glen Torridon unit of Gale Crater, Mars. *Journal of Geophysical Research: Planets*, 127(12), e2021JE007097. <https://doi.org/10.1029/2021JE007097>
- Gasda, P. J., Lanza, N., Rapin, W., Frydenvang, J., Goetz, W., Schwenzer, S. P., et al. (2023). ChemCam observations of the Marker Band, Gale crater, Mars. In *54th lunar and planetary science conference 2389*.
- Gellert, R., Clark, B. C., III, & Mars Science Laboratory (MSL) Science Team. (2015). In situ compositional measurements of rocks and soils with the Alpha Particle X-ray Spectrometer on NASA's Mars rovers. *Elements*, 11(1), 39–44. <https://doi.org/10.2113/gselements.11.1.39>
- Gellert, R., Rieder, R., Brückner, J., Clark, B. C., Dreibus, G., Klingelhöfer, G., et al. (2006). Alpha Particle X-Ray Spectrometer (APXS): Results from Gusev crater and calibration report. *Journal of Geophysical Research: Planets*, 111(E2), E02S05. <https://doi.org/10.1029/2005JE002555>
- Golombek, M., Grant, J., Kipp, D., Vasavada, A., Kirk, R., Ferguson, R., et al. (2012). Selection of the Mars Science Laboratory landing site. *Space Science Reviews*, 170(1–4), 641–737. <https://doi.org/10.1007/s11214-012-9916-y>
- Grotzinger, J. P., Crisp, J., Vasavada, A. R., Anderson, R. C., Baker, C. J., Barry, R., et al. (2012). Mars Science Laboratory mission and science investigation. *Space Science Reviews*, 170(1–4), 5–56. <https://doi.org/10.1007/s11214-012-9892-2>
- Grotzinger, J. P., Gupta, S., Malin, M. C., Rubin, D. M., Schieber, J., Siebach, K., et al. (2015). Deposition, exhumation, and paleoclimate of an ancient lake deposit, Gale Crater, Mars. *Science*, 350(6257), aac7575. <https://doi.org/10.1126/science.aac7575>
- Gupta, S., Dietrich, W. E., Lewis, K. W., Kite, E., Mondro, C. A., Schieber, J., et al. (2023). High but not so dry on Aeolis Mons: Transient Lake Systems in Hesperian Deserts in Gale crater. In *54th lunar and planetary science conference 2806*.

- Haber, J. T., Horgan, B., Fraeman, A. A., Johnson, J. R., Bell, J. F., III, Rice, M. S., et al. (2022). Mineralogy of a possible ancient lakeshore in the Sutton Island member of Mt. Sharp, Gale crater, Mars, from Mastcam multispectral images. *Journal of Geophysical Research: Planets*, 127(10), e2022JE007357. <https://doi.org/10.1029/2022JE007357>
- Hapke, B. (1993). *Theory of reflectance and emittance spectroscopy*. Cambridge University Press.
- Harris, J. K., & Grindrod, M. P. (2018). Hapke mixture modeling applied to VNIR spectra of mafic mineral mixtures and shergottites: Implications for quantitative analysis of satellite data. *Meteoritics & Planetary Sciences*, 53(6), 1179–1206. <https://doi.org/10.1111/maps.13065>
- Horgan, B. H. N., Johnson, J. R., Fraeman, A. A., Rice, M. S., Seeger, C., Bell, J. F., et al. (2020). Diagenesis of Vera Rubin ridge, Gale Crater, Mars, from Mastcam multispectral images. *Journal of Geophysical Research: Planets*, 125(11), e2019JE006322. <https://doi.org/10.1029/2019JE006322>
- Hoza, K. (2019). *Photometric investigations of weathering rinds and coatings with implications for Mars. (Unpublished master's dissertation)* (p. 921). WWU Graduate School Collection. Retrieved from <https://cedar.wvu.edu/wwuet/921>
- Jacob, S. R. (2022). *Deciphering the geologic history and mineralogy of Planets from Mars to exoplanets using rover in situ analysis (Doctoral dissertation)*. Laboratory Spectroscopy and Modeling, Arizona State University.
- Johnson, J. R., Bell, J. F., III, Bender, S., Blaney, D., Cloutis, E., DeFlores, L., et al. (2015). MSL Science Team, ChemCam passive reflectance spectroscopy of surface materials at the *Curiosity* landing site, Mars. *Icarus*, 249, 74–92. <https://doi.org/10.1016/j.icarus.2014.02.028>
- Johnson, J. R., Grundy, W. M., Lemmon, M. T., Liang, W., Bell, J. F., Hayes, A. G., & Deen, R. G. (2021). Spectrophotometric properties of materials observed by Pancam on the Mars Exploration Rovers: 4. Final mission observations. *Icarus*, 357, 114261. <https://doi.org/10.1016/j.icarus.2020.114261>
- Kling, A. M., Haberle, R. M., McKay, C. P., Bristow, T. F., & Rivera-Hernández, F. (2020). Subsistence of ice-covered lakes during the Hesperian at Gale crater, Mars. *Icarus*, 338, 113495. <https://doi.org/10.1016/j.icarus.2019.113495>
- Kotler, J. M. (2009). Biosignature storage in sulfate minerals-synthetic and natural investigations of the jarosite group minerals. In *Graduate student theses, dissertations, and professional papers 1275*. Retrieved from <https://scholarworks.umd.edu/etd/1275>
- Kraft, M. D., & Christensen, P. R. (2013). Tectonic formation of Mount Sharp, Gale crater, Mars. In *44th lunar and planetary science 3106*.
- Lane, M. D., Morris, R. V., Mertzman, S. A., & Christensen, P. R. (2002). Evidence for platy hematite grains in Sinus Meridiani, Mars. *Journal of Geophysical Research*, 107(E12), 9-1–9-15. <https://doi.org/10.1029/2001JE001832>
- Lapo, K. (2021). *Martian Spectroscopy: Laboratory calibration of the Perseverance rover's Mastcam-Z and photometric investigation of Mars-analog ferric-coated sand (Unpublished master's dissertation)*. WWU Graduate School Collection 1011. Retrieved from <https://cedar.wvu.edu/wwuet/1011>
- Lewis, K. W., Kite, E. S., Weitz, C. M., Cowart, A., Dietrich, W. E., Gupta, S., et al. (2023). Rhythmic stratigraphy at the orbital marker band at Mount Sharp, Gale crater, Mars. In *54th lunar and planetary science conference 2806*.
- Lynch, K. L., Horgan, B. H., Munakata-Marr, J., Hanley, J., Schneider, R. J., Rey, K. A., et al. (2015). Near-infrared spectroscopy of lacustrine sediments in the Great Salt Lake Desert: An analog study for Martian paleolake basins. *Journal of Geophysical Research: Planets*, 120(3), 599–623. <https://doi.org/10.1002/2014JE004707>
- Malin, M. C., Ravine, M. A., Caplinger, M. A., Tony Ghaemi, F., Schaffner, J. A., Maki, J. N., et al. (2017). The Mars Science Laboratory (MSL) mast cameras and descent imager: Investigation and instrument descriptions. *Earth and Space Science*, 4(8), 506–539. <https://doi.org/10.1002/2016EA000252>
- Maurice, S., Wiens, R., Saccoccio, M., Barraclough, B., Gasnault, O., Forni, O., et al. (2012). The ChemCam instrument suite on the Mars Science Laboratory (MSL) rover: Science objectives and mast unit description. *Space Science Reviews*, 170(1–4), 95–166. <https://doi.org/10.1007/s11214-012-9912-2>
- Michalski, J. R., Kraft, M. D., Sharp, T., & Christensen, P. (2006). Effects of chemical weathering on infrared spectra of Columbia River Basalt and spectral interpretations of Martian alteration. *Earth and Planetary Science Letters*, 248(3–4), 822–829. <https://doi.org/10.1016/j.epsl.2006.06.034>
- Milliken, R. E., Grotzinger, J. P., & Thomson, B. J. (2010). Paleoclimate of Mars as captured by the stratigraphic record in Gale Crater. *Geophysical Research Letters*, 37(4), 6. <https://doi.org/10.1029/2009GL041870>
- Mintiti, M. E., Rivera-Hernández, F., Bennett, K. A., Gupta, S., & Wiens, R. C. (2021). Rock textures and grain sizes in the Glen Torridon region (Gale Crater, Mars) observed by the Mars Hand Lens Imager (MAHLI) and ChemCam. In *52nd lunar and planetary science conference, no. 2435*.
- Moreras-Marti, A., Fox-Powell, M., Cousins, C. R., Macey, M. C., & Zerkle, A. L. (2022). Sulfur isotopes as biosignatures for Mars and Europa exploration. *Journal of the Geological Society*, 179(6), jgs2021-134. <https://doi.org/10.1144/jgs2021-134>
- Murchie, S. L., Mustard, J. F., Ehlmann, B. L., Milliken, R. E., Bishop, J. L., McKeown, N. K., et al. (2009). A synthesis of Martian aqueous mineralogy after 1 Mars year of observations from the Mars Reconnaissance Orbiter. *Journal of Geophysical Research*, 114(E2), E00D06. <https://doi.org/10.1029/2009JE003342>
- Niles, P. B., & Michalski, J. (2012). Origin and evolution of sediments in Gale crater through ice-hosted processes. In *Lunar and planetary science conference 2012 no. 2575*.
- Paramanick, S., Rajesh, V. J., Praveen, M. N., Sajinkumar, K. S., & Bhattacharya, S. (2021). Spectral and chemical characterization of Copiapite and Rozenite from Padminjarathara in Wayanad, southern India: Implications for Mars exploration. *Chemical Geology*, 575, 120043. <https://doi.org/10.1016/j.chemgeo.2020.120043>
- Pedregosa, F., Varoquax, G., Gramfort, A., Michel, V., & Thirion, B. (2011). Scikit-learn: Machine learning in Python. *Journal of Machine Learning Research*, 12, 2825–2830.
- Rampe, E. B., Bristow, T. F., Blake, D. F., Chipera, S. J., Vaniman, D. T., Achilles, C. N., et al. (2023). Mineralogical evidence for environmental change in the CST at Gale crater, Mars. In *54th lunar and planetary science conference, 1554*.
- Rapin, W., Dromart, G., Rubin, D., Deit, L. L., Mangold, N., Edgar, L. A., et al. (2021). Alternating wet and dry depositional environments recorded in the stratigraphy of Mount Sharp at Gale crater, Mars. *Geology*, 49(7), 842–846. <https://doi.org/10.1130/G48519.1>
- Rapin, W., Dromart, G., Schieber, J., Clark, B. C., Kah, L., Rubin, D., et al. (2023). Not always wet: An aridification sequence in the orbital CST of Aeolis Mons. In *54th lunar and planetary science conference, 2806*.
- Rapin, W., Ehlmann, B. L., Dromart, G., Schieber, J., Thomas, N. H., Fischer, W. W., et al. (2019). An interval of high salinity in ancient Gale crater lake on Mars. *Nature Geoscience*, 12(11), 889–895. <https://doi.org/10.1038/s41561-019-0458-8>
- Rice, M. S. (2022). Mastcam multispectral database from the *Curiosity* rover's traverse in Gale crater, Mars (sols 0–2302) [Dataset]. WWU Geology Faculty Publications, 104. <https://doi.org/10.25710/rqr0-8x75>
- Rice, M. S., Bell, J. F., Cloutis, E. A., Wang, A., Ruff, S. W., Craig, M. A., et al. (2010). Silica-rich deposits and hydrated minerals at Gusev Crater, Mars: Vis-NIR spectral characterization and regional mapping. *Icarus*, 205(2), 375–395. <https://doi.org/10.1016/j.icarus.2009.03.035>

- Rice, M. S., Cloutis, E., Bell, J., Bish, D., Horgan, B., Mertzman, S., et al. (2013). Reflectance spectra diversity of silica-rich materials: Sensitivity to environment and implications for detections on Mars. *Icarus*, 223(1), 499–533. <https://doi.org/10.1016/j.icarus.2012.09.021>
- Rice, M. S., Johnson, J. R., Million, C. C., St. Clair, M., Horgan, B. N., Vaughan, A., et al. (2023). Spectral variability of rocks and soils on the Jezero crater floor: A summary of multispectral observations from Perseverance's Mastcam-Z instrument. *Journal of Geophysical Research: Planets*, 128(10), e2022JE007548. <https://doi.org/10.1029/2022JE007548>
- Rice, M. S., Seeger, C., Bell, J., Calef, F., St. Clair, M., Eng, A., et al. (2022). Spectral diversity of rocks and soils in Mastcam observations along the Curiosity rover's traverse in Gale crater, Mars. *Journal of Geophysical Research: Planets*, 127(8), e2021JE007134. <https://doi.org/10.1029/2021JE007134>
- Rieder, R., Gellert, R., Brückner, J., Klingelhöfer, G., Dreibus, G., Yen, A., & Squyres, S. W. (2003). The new Athena alpha particle X-ray spectrometer for the Mars Exploration Rovers. *Journal of Geophysical Research, Planets*, 108(E12), 8066. <https://doi.org/10.1002/2015GL066675>
- Rietveld, H. (1969). A profile refinement method for nuclear and magnetic structures. *Journal of Applied Crystallography*, 2(2), 65–71. <https://doi.org/10.1107/s0021889869006558>
- Rivera-Hernández, F., Sumner, D. Y., Mangold, N., Banham, S. G., Edgett, K. S., Fedo, C. M., et al. (2020). Grain size variations in the Murray formation: Stratigraphic evidence for changing depositional environments in Gale crater, Mars. *Journal of Geophysical Research: Planets*, 125(2), e2019JE006230. <https://doi.org/10.1029/2019JE006230>
- Roberts, A. L., Gupta, S., Dietrich, W. E., Edgar, L. A., Rapin, W., Banham, S. G., et al. (2023). What depositional processes and paleoenvironments formed the layered sulfate unit in Gale crater, Mars? Insights from Marker Band valley. In *54th lunar and planetary science conference*, 2806.
- Roush, T. L., Bishop, J. L., Brown, A. J., Blake, D. F., & Bristow, T. F. (2015). Laboratory reflectance spectra of clay minerals mixed with Mars analog materials: Toward enabling quantitative clay abundances from Mars spectra. *Icarus*, 258, 454–466. <https://doi.org/10.1016/j.icarus.2015.06.035>
- Rudolph, A., Horgan, B., Johnson, J., Bennett, K., Haber, J., Bell, J. F., et al. (2022). The distribution of clay minerals and their impact on diagenesis in Glen Torridon, Gale crater, Mars. *Journal of Geophysical Research: Planets*, 127(10), e2021JE007098. <https://doi.org/10.1029/2021JE007098>
- Schwertmann, U., & Murad, E. (1983). Effect of pH on the formation of goethite and hematite from ferrihydrite. *Clays and Clay Minerals*, 31(4), 277–284. <https://doi.org/10.1346/CCMN.1983.0310405>
- Seeger, C. H. (2020). *Using multispectral imagery to interrogate deposition, alteration, and weathering across Curiosity rover's traverse in Gale crater, Mars (Unpublished master's dissertation)*. WWU Graduate School Collection 974. Retrieved from <https://cedar.wvu.edu/wwuet/974>
- Seeger, C. H., Grotzinger, J. P., & Cowart, A. C. (2023). Diagenetic overprints associated with the CST in Gale crater, Mars. In *54th lunar and planetary science conference*, 2806.
- Sheppard, R. Y., Milliken, R. E., Parente, M., & Itoh, Y. (2021). Updated perspectives and hypotheses on the mineralogy of lower Mt. Sharp, Mars, as seen from orbit. *Journal of Geophysical Research: Planets*, 126(2), e2020JE006372. <https://doi.org/10.1029/2020JE006372>
- Sheppard, R. Y., Milliken, R. E., & Robertson, K. M. (2022). Presence of clay minerals can obscure spectral evidence of Mg sulfates: Implications for orbital observations of Mars. *Icarus*, 383, 115083. <https://doi.org/10.1016/j.icarus.2022.115083>
- Sheppard, R. Y., Thorpe, M. T., Fraeman, A. A., Fox, V. K., & Milliken, R. E. (2021). Merging perspectives on secondary minerals on Mars: A review of ancient water-rock interactions in Gale crater inferred from orbital and in-situ observations. *Minerals*, 11(9), 986. <https://doi.org/10.3390/min11090986>
- Shkuratov, Y., Starukhina, L., Hoffmann, H., & Arnold, G. (1999). A model of spectral albedo of particulate surfaces: Implications for optical properties of the Moon. *Icarus*, 137(2), 235–246. <https://doi.org/10.1006/icar.1998.6035>
- Simpson, S. L., Achilles, C. N., Rampe, E. B., Bristow, T. F., Blake, D. F., Chipera, S. J., et al. (2023). The composition of X-ray amorphous materials in Gale crater, Mars. In *54th lunar and planetary science conference*, 2781.
- Sklute, E. C., Jensen, H. B., Rogers, A. D., & Reeder, R. J. (2015). Morphological, structural, and spectral characteristics of amorphous iron sulfates. *Journal of Geophysical Research: Planets*, 120(4), 809–830. <https://doi.org/10.1002/2014JE004784>
- Smith, R. J., McLennan, S. M., Achilles, C. N., Dehouck, E., Horgan, B. H. N., Mangold, N., et al. (2021). X-ray amorphous components in sedimentary rocks of Gale crater, Mars: Evidence for ancient formation and long-lived aqueous activity. *Journal of Geophysical Research: Planets*, 126(3), e2020JE006782. <https://doi.org/10.1029/2020JE006782>
- Smith, R. J., McLennan, S. M., Sutter, B., Rampe, E. B., Dehouck, E., Siebach, K. L., et al. (2022). X-ray amorphous sulfur-bearing phases in sedimentary rocks of Gale crater, Mars. *Journal of Geophysical Research: Planets*, 127(5), e2021JE007128. <https://doi.org/10.1029/2021JE007128>
- Stack, K. M., & Milliken, R. E. (2015). Modeling near-infrared reflectance spectra of clay and sulfate mixtures and implications for Mars. *Icarus*, 250, 332–356. <https://doi.org/10.1016/j.icarus.2014.12.009>
- Thompson, L. M., Spray, J., Gellert, R., Williams, R., Berger, J., O'Connell-Cooper, C., et al. (2022). APXS-determined compositional diversity of eolian Siccac Point group sandstones, Gale crater Mars: Implications for provenance and timing of events. In *EPSC2022-1184*. <https://doi.org/10.5194/epsc2022-1184>
- Thompson, L. M., Kite, E. S., Grotzinger, J. P., Yen, A. S., Berger, J. A., Lewis, K. W., et al. (2023). Investigation of the Gale crater marker band (and beyond) with the Mars Science Laboratory, alpha particle X-ray spectrometer. In *54th lunar and planetary science conference*, 2806.
- Thompson, L. M., Spray, J. G., O'Connell-Cooper, C., Berger, J. A., Yen, A., Gellert, R., et al. (2022). Alteration at the base of the Siccac Point unconformity and further evidence for an alkaline provenance at Gale crater: Exploration of the Mount Sharp group, Greenheugh pediment cap rock contact with APXS. *Journal of Geophysical Research: Planets*, 127(11), e2021JE007178. <https://doi.org/10.1029/2021JE007178>
- Thomson, B. J., Buczkowski, D. L., Crumpler, L. S., Seelos, K. D., & Fassett, C. I. (2019). How much of the sediment in Gale crater's central mound was fluviially transported? *Geophysical Research Letters*, 46(10), 5092–5099. <https://doi.org/10.1029/2018GL081727>
- Thorpe, M. T., Bristow, T. F., Rampe, E. B., Tosca, N. J., Grotzinger, J. P., Bennett, K. A., et al. (2022). Mars Science Laboratory CheMin data from the Glen Torridon region and the significance of lake-groundwater interactions in interpreting mineralogy and sedimentary history. *Journal of Geophysical Research: Planets*, 127(11), e2021JE007099. <https://doi.org/10.1029/2021JE007099>
- Turenne, N., Sidhu, S., Applin, D. M., Cloutis, E. A., Wolf, Z. U., Mertzman, S. A., et al. (2023). Spectral reflectance properties of nontronite exposed to Mars-like surface conditions and low-temperature heating (<300°C). *Icarus*, 395, 115448. <https://doi.org/10.1016/j.icarus.2023.115448>
- Vaniman, D. T., Bish, D. L., Chipera, S. J., Fialips, C. I., William Carey, J., & Feldman, W. C. (2004). Magnesium sulphate salts and the history of water on Mars. *Nature*, 431(7009), 663–665. <https://doi.org/10.1038/nature02973>
- Vasavada, A. R. (2022). Mission overview and scientific contributions from the Mars Science Laboratory Curiosity rover after eight years of surface operations. *Space Science Reviews*, 218(3), 14. <https://doi.org/10.1007/s11214-022-00882-7>

- Wang, A., Freeman, J. J., & Jolliff, B. L. (2009). Phase transition pathways of the hydrates of magnesium sulfate in the temperature range 50°C to 5°C: Implication for sulfates on Mars. *Journal of Geophysical Research*, *114*(E4), E04010. <https://doi.org/10.1029/2008JE003266>
- Wang, A., Jolliff, B. L., Liu, Y., & Connor, K. (2016). Setting constraints on the nature and origin of the two major hydrous sulfates on Mars: Monohydrated and polyhydrated sulfates. *Journal of Geophysical Research: Planets*, *121*(4), 678–694. <https://doi.org/10.1002/2015JE004889>
- Watkins, J. A., Grotzinger, J. P., Stein, N. T., Banham, S. G., Gupta, S., Rubin, D. M., et al. (2022). Burial and exhumation of sedimentary rocks revealed by the base stimson erosional unconformity, Gale crater, Mars. *Journal of Geophysical Research: Planets*, *127*(7), e2022JE007293. <https://doi.org/10.1029/2022je007293>
- Weitz, C. M., Lewis, K. W., Bishop, J. L., Thomson, B. J., Arvidson, R. E., Grant, J. A., et al. (2022). Orbital observations of a marker horizon at Gale crater. *Journal of Geophysical Research: Planets*, *127*(4), e2022JE007211. <https://doi.org/10.1029/2022JE007211>
- Weitz, C. M., Lewis, K. W., Kite, E. S., Dietrich, W. E., Thompson, L. M., O'Connell, C. D., et al. (2023). The marker band in Gale crater: A synthesis of orbital and ground. In *54th lunar and planetary science conference, 2806*.
- Wellington, D. F., Johnson, J. R., Meslin, P. Y., & Bell, J. F., III. (2018). Iron meteorite candidates within Gale crater, Mars, from MSL/Mastcam multispectral observations. In *49th lunar and planetary science conference*.
- Wiens, R. C., Maurice, S., Barraclough, B., Saccoccio, M., Barkley, W. C., Bell, J. F., et al. (2012). The ChemCam instrument suite on the Mars Science Laboratory (MSL) Rover: Body Unit and combined system tests. *Space Science Reviews*, *170*(1), 167–227. <https://doi.org/10.1007/s11214-012-9902-4>
- Xu, W., & Parise, J. B. (2012). Temperature and humidity effects on ferric sulfate stability and phase transformation. *American Mineralogist*, *97*(2–3), 378–383. <https://doi.org/10.2138/am.2012.3927>
- Yu, X., Zhao, Y., Wu, Y., Qi, C., Li, D., Honglei, L., et al. (2022). Cryogenic sulfuric weathering and challenges for preserving iron-rich olivine on cold and icy Mars. *Journal of Geophysical Research: Planets*, *128*(1), e2022JE007593. <https://doi.org/10.1029/2022JE007593>
- Zolotov, M. Y., & Mironenko, M. V. (2007). Timing of acid weathering on Mars: A kinetic-thermodynamic assessment. *Journal of Geophysical Research*, *112*(E7), E07006. <https://doi.org/10.1029/2006JE002882>